The Pennsylvania State University

The Graduate School

ASSESSMENT AND IMPROVEMENT OF FLOW QUALITY IN A SMALL FOOTPRINT ADDITIVELY MANUFACTURED WIND TUNNEL

A Thesis in

Mechanical Engineering

by

Niveditha Sappa Veena Venkata

Submitted in Partial Fulfillment
of the Requirements
for the Degree of

Master of Science

August 2024

The thesis of Niveditha Sappa Veena Venkata was reviewed and approved by the following:

Tamy Guimarães
Assistant Professor of Mechanical Engineering
Thesis Advisor

Robert Kunz
Professor of Mechanical Engineering

Mary Frecker
Professor of Mechanical Engineering
Department Head of Mechanical Engineering

ABSTRACT

Achieving optimal flow quality is a priority in assessing the performance of wind tunnels, especially in low-speed applications. This thesis presents an approach to improving flow quality in a low-speed wind tunnel by incorporating additive manufactured connectors (flanges) at locations identified with gaps, misalignment, and orientation issues. Six flanges were strategically placed at both ends of the test section and contraction side in pairs. These modifications are aimed at reducing flow disruptions and enhancing flow uniformity, which are critical for accurate and reliable aerodynamic testing. Improved flow stability and uniformity are essential in wind tunnels for accurate and repeatable aerodynamic testing and should provide a controlled environment where airflow closely simulates real-world conditions, enabling precise measurement of aerodynamic properties. The effectiveness of these modifications was assessed through the analysis of velocity profiles and turbulence intensity at different locations along the wind tunnel test section. Experimental data were gathered from pressure readings obtained using pitot-static tubes connected to a Scanivalve pressure scanner and converted to velocity values using Bernoulli's equation. The obtained data were compared before and after the integration of these flanges. Results indicated a significant improvement in flow uniformity and a decrease in turbulence intensity post-intervention. Moreover, the velocity profiles exhibited a more consistent and predictable behavior, indicative of improved flow stability. These findings address the flow quality concerns within the low-speed wind tunnel setups, offering insights for optimizing performance in various aerodynamic testing environments.

TABLE OF CONTENTS

LIST OF FIGURES

LIST OF TABLES

ACKNOWLEDGEMENTS

I would like to express my deepest gratitude to all those who have supported and guided me throughout the journey of completing this master's thesis. First and foremost, I extend my sincere thanks to my advisor, Dr. Tamy Guimarães for her invaluable guidance, insightful feedback, and support throughout this research endeavor, which has been truly inspiring. I also wish to thank my thesis committee member, Dr. Robert Kunz, for his insightful advice, which greatly enhanced the quality of this work and for providing financial support through graduate assistantships throughout my degree. A special thanks to the faculty and staff of the Mechanical Engineering at Pennsylvania State University for their resources, support, and enriching experiences I was provided with as an international student.

To my parents, their unwavering love, encouragement, and belief in me have been my foundation. My appreciation also extends to my sister Jnanitha, my friends Stephen and Aneesh, for always being there for me and morally boosting my confidence. Also, my heartful gratitude to my fellow graduate students, and friends from India, your support and hangouts have made this journey more manageable and enjoyable. I deeply value our shared experiences and lasting friendships. Finally, I thank all my lab mates and collaborators, especially Muhannad who contributed to this research. Your willingness to share your time and experiences has been invaluable.

Chapter 1

Overview of Wind Tunnels and Research Motivation

Wind Tunnels: An overview

Ever since the first wind tunnel was built to understand air flow over aircraft surfaces to better understand flight, major technological advancements in the field of wind tunnel testing have paved the way for their applications to expand. This expansion includes testing membrane roofs for civil engineering [1], studying soils and natural surfaces [2], investigating the drying mechanisms in solids [3], examining pollutant plume dispersion [4], and assessing athletes' aerodynamic drag [5], to name a few. It is noteworthy to highlight the different types of wind tunnels being used based on the speed, configuration, output, and applications. Most commonly they are classified based on the range of speed as subsonic or low-speed wind tunnels (Mach < 0.8), transonic (Mach 0.8 – 1.2), supersonic (Mach 1.2 – 5.0), and hypersonic (Mach >5.0). Here, the term Mach refers to the local speed of air relative to the speed of sound [6].

Furthermore, low-speed wind tunnels are categorized as open and closed [7], [8]. Air in an open circuit tunnel traverses a linear trajectory, entering through a contraction to reach the test section. Subsequently, it passes through a diffuser, and a fan section located downstream, which uses suction to draw air through the wind tunnel. In contrast, if air is blown down in the tunnel by a blower located upstream of the test- section, it creates another configuration of open circuit tunnel called blow-down wind tunnels. Though open circuit wind tunnels have lower fabrication costs and a smaller footprint, they demand more energy for operation. In closed-circuit wind tunnels, on the other hand, the air circulates in a continuous loop, experiencing minimal to no exchange with the external environment. Despite higher construction costs, they offer lower operating expenses, but the choice between open and closed circuits depends on the experiment-specific requirements,

considering the balance between initial setup costs and long-term operational efficiency in research [9]. Based on these factors and constraints, this research focuses on a low-speed, open-circuit wind tunnel because it better serves the needs of university research by being cost-effective and small-scale.

Wind tunnels vs CFD: Technological Impact

The introduction of Computational Fluid Dynamics (CFD) has been proven to be a revolutionary tool for fluid dynamics due to its flexibility in changing data, response speed, and portability [10], [11]. While CFD has indeed emerged as a powerful tool in aerodynamic research and engineering design, it does not simply replace wind tunnel testing. It rather complements it. Though CFD offers several advantages, including cost-effectiveness, flexibility in simulating various conditions, and the ability to analyze complex flow phenomena, it also faces challenges, particularly in accurately capturing scale effects, such as Reynolds number effects, and modeling geometrically simple yet complex behaving systems [12]. This requires the development of new methods and software for discussing scaling effects [13]. Even after validating physical and mathematical models, as well as verifying numerical solutions, there is a notable gap in applying these guidelines to real engineering scenarios. Hence it is necessary to be aware of potential shortcomings in CFD simulations.

Moreover, CFD can also be used for conceptual design, prototyping, and exploring new ideas rather than relying on it without building the physical model. It is preferable to use the combination of experimental and CFD since they would be an effective tool in conjunction to better attain results and compare.

Aerodynamics of the Wind Tunnel

Wind tunnel aerodynamics, especially for low-speed wind tunnels, which is this project's interest, involves understanding the fundamental principles and equations that are involved in the flow behavior in the wind tunnel [6]. This section delves into key principles and concepts such as the Navier-Stokes equations, Mach and Reynolds numbers, and boundary layer behavior. Additionally, it covers fundamental aerodynamic lift and drag forces. These concepts are crucial for understanding and analyzing flow behavior within the wind tunnel, ensuring accurate and reliable testing results. By comprehending these principles, a better interpretation of data, improved design and performance of the wind tunnel can be achieved.

Navier-Stokes Equations

Derived from the principles of conservation of mass, momentum, and energy, Navier-Stokes equation [14] is a system of partial differential equations that describe the fluid motion in space. The Navier-Stokes equations are nonlinear; their terms do not follow a simple linear relationship, which requires advanced methods for solving. This nonlinearity is essential for modeling complex fluid dynamics like shock waves, making the equations more challenging to solve.

The Navier-Stokes equation can be solved based on several simplifying assumptions: continuous fluid with density ρ, velocity v, and pressure p, negligible temperature fluctuations, stress tensor (defined below) follows a constitutive law for a Newtonian fluid, an equation of state relation exists between p and ρ [15].

General Navier-Stokes Equation: $\rho \frac{Dv}{Dt} = \rho \left(\frac{\partial v}{\partial t} + v \cdot \nabla v \right) = -\nabla p + \nabla \cdot \tau + f$, where ρ = fluid density, $\frac{Dv}{Dt}$ = acceleration of a fluid particle, $\frac{\partial v}{\partial t}$ = Local acceleration, $v \cdot \nabla v$ = convective

acceleration, change in velocity due to the motion of the fluid, $-\nabla p$ = pressure gradient force, $\nabla \cdot \tau$ = divergence of the stress tensor, force due to viscous effects, f = External body forces.

For Compressible Newtonian Fluid: $\rho \frac{Dv}{Dt} = \rho\left(\frac{\partial v}{\partial t} + v \cdot \nabla v\right) = -\nabla p + \frac{1}{3}\mu\big(\nabla(\nabla \cdot v)\big) + \mu\nabla^2 v + f$, where $\frac{1}{3}\mu\big(\nabla(\nabla \cdot v)\big)$ = bulk viscosity term, accounts for compressibility effects, $\mu\nabla^2 v$ = viscous term, describes viscous diffusion of momentum.

For Incompressible Newtonian Fluid: $\rho \frac{Dv}{Dt} = \rho\left(\frac{\partial v}{\partial t} + v \cdot \nabla v\right) = -\nabla p + \mu\nabla^2 v + f$, where ρ = fluid density, which may vary for compressible fluids but is constant for incompressible fluids, $\frac{Dv}{Dt}$ = acceleration of a fluid particle, $\frac{\partial v}{\partial t}$ = Local acceleration, $v \cdot \nabla v$ = convective acceleration, $-\nabla p$ = pressure gradient force, $\nabla \cdot \tau$ = viscous stress term, μ = dynamic viscosity, $\nabla^2 v$ = Laplacian of velocity, f = External body forces.

Reynolds Number (Re) and Mach Number (M)

The Reynolds number (Re) [16] is a dimensionless quantity, defined as the ratio of inertial forces to viscous forces, and is used to predict the flow patterns in different fluid flow situations. $Re = \rho \cdot V \cdot L / \mu$, where ρ is the air density, V is the velocity, L is a characteristic length, and μ is dynamic viscosity. The Reynolds number helps predict flow patterns - laminar or turbulent, since different flow regimes affect the aerodynamic forces acting on the model and, consequently, its performance. To ensure that test results from a scaled-down model are applicable to the real object, the Reynolds number for both the model and the full-scale object should match. This matching ensures that the flow patterns around the model are dynamically similar to those around the actual object.

Mach number (M) [16] is a dimensionless quantity as defined in Chapter 1, M = V /a, where V is the velocity of the fluid, and a is the speed of sound. The Mach number indicates whether

the flow is compressible or not. Typically, below Mach 0.3 the flow behaves as incompressible. However, as the Mach number increases, compressibility effects become significant, influencing pressure distributions and shock waves formation. Since Mach number is used to characterize different flow regimes (subsonic, transonic, supersonic, and hypersonic), matching the Mach number in tests ensures that these phenomena are correctly reproduced to exhibit distinct aerodynamic phenomena.

Similarity parameters like Reynolds and Mach numbers ensure that wind tunnel tests on scaled models reflect real-world conditions accurately. Matching these parameters guarantees consistent flow patterns between the model and the full-scale object, enabling researchers to reliably predict actual object behavior and optimize designs effectively. Though these two parameters are completely different, for stationary model experiments during data gathering, the Reynolds number and Mach number are pivotal similarity parameters. In cases where the model and full-scale applications have the same Reynolds and Mach numbers, then both flows will be dynamically similar.

Boundary Layer

The air or water flowing around an object moves at the same speed as the object due to viscosity effects. Yet, there is a small region relative to the overall size of the object where there is a noticeable change in velocity, called the boundary layer, shown in Figure 1-1. This high gradient layer has a velocity resembling that in a potential flow around a similar object where there is no separation [16], [17]. In simple words, flow particles closest to the surface of the object stick to it as it passes over; this is called a “no slip condition”, where the velocity at the surface is zero. As these flow particles move away from the surface, the velocity slowly rises from zero and reaches the free stream velocity. The formation of a thin layer with a velocity gradient from zero to the free

stream velocity is the boundary layer. Wind tunnel aerodynamics often involves studying and manipulating the boundary layer to optimize aerodynamic performance since it affects drag and heat transfer.

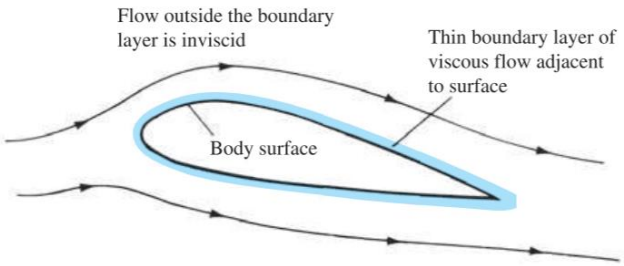

Figure **1-1**: Boundary layer formed at the surface of a body is represented by the blue region [17].

Aerodynamic Forces

Any object moving through a fluid experiences aerodynamic forces and moments due to two basic sources: pressure and shear stress distribution of the body surface [17]. The resultant shear and pressure forces can be split into two components: Lift (direction normal to the flow) and Drag (direction of the flow) as shown in in Figure 1-2. Due to the combined effects of the pressure and wall shear components, the lift force tends to move the body up while the drag force pushes the body in the flow direction [16]. Usually, drag is an undesirable component and is always tried to minimize it. Wind tunnel testing includes measuring lift and drag forces acting on an object, as described in Appendix A. Lift measurements are used to assess the uniformity of the flow and provide insights into the aerodynamic stall conditions of the object in the wind tunnel. Whereas anomalies in the drag help indicate the quality of the flow and issues with boundary layer separation.

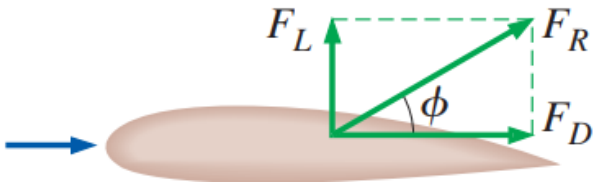

Figure **1-2**: Relative wind (blue arrow) flowing over an airfoil structure, generating resultant aerodynamic forces (F_R): Lift (F_L) and Drag (F_D) [16].

Chapter 2

Flow Quality Requirements & Measurement

In the complex field of experimental fluid dynamics, accurate and reliable results depend upon a critical factor – flow quality. The effectiveness of wind tunnels lies not only in their design and instrumentation but equally relies on high flow quality. Understanding the parameters, requirements, and methodologies for assessing flow quality plays a pivotal role in assessing the success of the experiments, ensuring that the simulated conditions replicate real-world applications.

Parameters Assessing Flow Quality

The quality of the flow within a wind tunnel is estimated based on the changes observed in certain key parameters – turbulent velocity (vorticity), pressure (noise), and temperature (entropy) [18].

Velocity

In wind tunnels, achieving optimal flow quality involves carefully managing velocity. For velocity, it is crucial to ensure the flow speed is consistent across the entire test section is uniform, which guarantees the conditions experienced by the test object are the same throughout, leading to accurate aerodynamic testing [19]. Predictable velocity allows for reliable and repeatable experiments, making it possible to validate results. Steady velocity, where the flow does not fluctuate over time, ensures that the exposure to constant conditions, resulting in precise measurements and analyses.

Pressure (Noise)

Pressure fluctuations are variations in air pressure within the wind tunnel, often called noise. At low speeds, the pressure variations are quite small and have no significant effect. Most of the fluctuations are caused by turbulence.

Temperature (Entropy)

Variations in the thermal energy of the air within the wind tunnel lead to changes in entropy, a measure of disorder or randomness in the system. Temperature fluctuations can affect the density of the air, influencing the aerodynamic characteristics of the flow. Evaluating these irregularities ensures that the thermal environment remains stable, which is crucial for maintaining consistent and reliable flow conditions.

Several experiments conducted across the wind tunnel testing community [18], [20], [21] indicate the above parameters are in turn affected by higher wind tunnel velocities, poor tunnel design, turbulent boundary layer, changes in the environment, or other external factors, such as higher ambient temperatures, inefficient cooling systems, and heat generated by the tunnel's mechanical components. Additionally, understanding the fluctuations in these parameters helps in optimizing the design and operation of the wind tunnel to meet the desired testing conditions and obtain reliable experimental results.

Wind Tunnel Flow Irregularities

The accuracy of wind tunnel experiments can be compromised by various flow irregularities due to factors such as the geometry of the flow domain, imperfections in the

surfaces, and interactions with the surrounding environment. These irregularities, though diverse, broadly fall under – spatial non-uniformities, swirl, low-frequency unsteadiness, and turbulence [18].

Spatial Non-uniformities

Non-uniform variation in the mean velocity within the tunnel cross section refers to spatial nonuniformities [22]. Occasionally the air does not flow evenly through the tunnel, it may be faster at one place and slower at the other, which results in varying velocities. This problem is overcome by managing the head, which involves redistributing the pressure energy from regions of higher velocity to regions of lower velocity. “Head" represents the energy per unit weight of the fluid, often expressed in terms of pressure head (related to fluid pressure) or velocity head (related to fluid speed) [23]. This energy transfer helps to even out the flow, creating a more uniform velocity profile across the tunnel. These non-uniformities can surface due to imperfect design such as sharp corners, irregular changes in the area of cross-section, and inlet-outlet configurations. Obstacles in the form of support structures or instrumentation in the wind tunnel can create irregular airflow in the wind tunnel as well.

Swirl

The rotational component, or the spinning of the flow, can lead to variations in the direction of the flow due to the angular momentum introduced to the air circulating in the wind tunnel [22]. It is evident this undesirable effect is the result of non-streamlined flow due to asymmetries in inlet conditions or irregularly shaped diffuser of the wind tunnel. To overcome this problem, a better

design of all the connecting parts to minimize swirl generation and honeycomb structures as flow conditioning devices are employed.

Low-Frequency Unsteadiness

Low-frequency unsteadiness refers to periodic variations in the mean velocity in a flow. Identifying the root cause of these surges proves to be challenging. Additionally, these pulsations hinder the establishment of steady flow. This phenomenon is usually caused by disturbances in the wind tunnel environment, such as changes in temperature, pressure, or other external factors. It can also result from flow separation and reattachment on the model surfaces.

Turbulence

Turbulence is a phenomenon in fluid dynamics, giving rise to irregular and chaotic fluctuations in velocity over time [24]. Essentially, turbulence generates small vortices of different sizes and intensities which disrupt the fluid flow velocity by inducing swirling patterns and unpredictable fluctuations. It can be described as the unpredictable oscillations of velocity superimposed onto the average flow. Though this is a naturally occurring phenomenon in fluid flow, it can have impending effects on the performed experiments [22], [25], this irregularity can be solved through a combination of wind tunnel design improvements, correct calibration, and the use of measurement tools, screens, and diffusers to improve flow quality. Addressing turbulence with careful monitoring and adjustment is essential to obtain reliable and consistent performance of the wind tunnel.

Managing turbulence involves aiming for low turbulence intensity, minimal vorticity, and the ability to control turbulence levels when necessary. The effect of turbulence on the flow is

measured through a parameter called turbulence intensity, which is a measure of how much the velocity of fluid particles varies from the average flow velocity [9]. Low turbulence intensity, which refers to small fluctuations in the flow velocity, ensures a smoother flow that minimizes disturbances around the test object. Minimal vorticity, indicating low local rotation in the fluid, helps achieve laminar flow. Additionally, the ability to introduce and manage specific levels of controlled turbulence is important for simulating real-world applications.

Flow Measurement Techniques

In low-speed wind tunnels, various flow measurement tools are used to assess and quantify the characteristics of airflow, especially velocity [26], [27]. Velocity measurement techniques are broadly classified into three groups: pressure measurements, anemometry, and optical methods [19].

Pressure Measurements

Most wind tunnel testing techniques involve determining the velocity of the flow indirectly by measuring the static and stagnation pressures. The combination of pressure probes and transducers for measuring different pressures is the most commonly used wind tunnel testing technique [19].

Pitot Tubes [16]

A simple pitot tube has one hole at the front of a cylindrical tube placed parallel to the flow, connected to a pressure transducer to measure stagnation pressure only as in Figure 2-1. Since pitot tubes measure only the stagnation pressure, separate static ports need to be installed elsewhere for

measuring static pressure. Hence, commercially Pitot-static tubes are being used which come with two openings to measure static and stagnation pressure.

Pitot Static Tubes

Pitot-static tubes consist of an opening directly facing the airflow which measures the stagnation pressure (total pressure) and side openings to measure the static pressure of the flow, each connected to the two ends of the pressure transducer as shown in Figures 2-1 and 2-2. When the airflow hits the probe, it comes to a complete stop at the probe opening resulting in an increased pressure (stagnation pressure). The transducer measures the difference between stagnation and static pressure, to yield dynamic pressure, which is used to calculate velocity using the Bernoulli Equation. This is calculated as: stagnation pressure – static pressure = ½ * density * velocity.

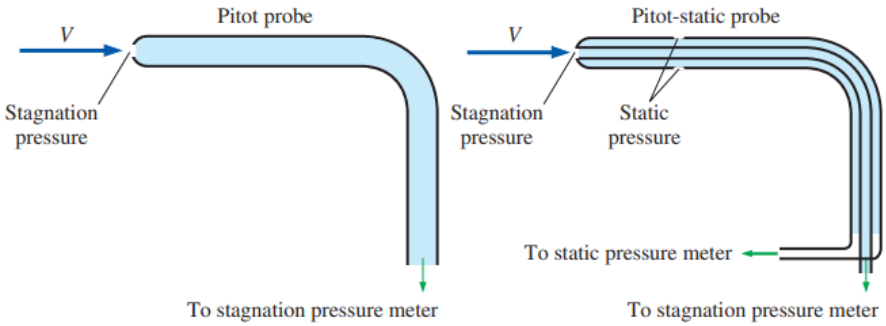

Figure **2-1**: A Pitot probe (left) measures stagnation pressure at the nose of the probe, while a Pitot-static probe (right) measures both stagnation pressure and static pressure [16].

Figure **2-2**: A detailed view of a Pitot-static probe reveals the presence of a stagnation pressure hole along with two static circumferential pressure holes [16].

Scanivalve Pressure Scanner

The Scanivalve pressure measurement device houses silicon piezoresistive pressure transducers, operating on the principle where electrical resistance changes in response to mechanical stress. The ports on the Scanivalve DSA3217 series pressure scanner (Figure 2-3) are connected via flexible pressure tubing to the pitot-static probe. The pressure scanner rapidly cycles through inputs from the pitot probe, converting analog pressure signals into digital data using an analog-to-digital converter. A microprocessor processes this data, adjusts for temperature variations, and converts it into pressure readings. By measuring total and static pressures, the pitot probe allows the pressure scanner to compute dynamic pressure by subtracting static pressure from total pressure. Processed data is transmitted via Ethernet to a computer or data acquisition system for monitoring, analysis, and storage.

Figure **2-3**: DSA3217 Scanivalve used for pressure measurements (taken from the DSA-PTP-datasheet).

Anemometry

Anemometry methods are based on direct measurement of flow velocity and formation of velocity vector fields. Anemometers have always been used extensively in weather stations because

of their capability to measure wind speed and direction. Initially, the most basic cup and vane anemometers were used and with the introduction of new technology modern techniques such as Laser Doppler anemometry, hot wire and film anemometry, and acoustic anemometry [16], [19].

Cup and Vane Anemometers

A simple cup anemometer looks like cups mounted at the tips of helicopter blades. Air flowing past these cups in any horizontal direction rotates the shaft the cups are mounted on. The rate of the shaft's revolutions over time is directly proportional to the wind's speed in cup anemometers.

Another version of anemometers was replacing the cups with vanes which makes the anemometer look like a windmill or a propeller as indicated in Figure 2-4. A vane anemometer has a propeller and a tail to cater for wind direction change and hence it is used to measure both wind speed and direction.

Figure **2-4**: A vane anemometer positioned at the wind tunnel test section [25].

Laser Doppler Anemometry (LDA)

Laser Doppler Anemometry (LDA) utilizes the Doppler shift to measure fluid velocity. When a laser beam is directed into a fluid flow, it interacts with particles in motion (due to the fluid flow), and the frequency of the scattered light changes as shown in Figure 2-5 and 2-6. This change in frequency is directly related to the velocity of the flow particles, and thus, the velocity of the

fluid flow. By measuring this frequency shift, LDA can determine the velocity of the flow at specific points within the measurement region. LDA is advantageous because it's a non-contact method and does not require calibration. However, it can be an expensive affair to acquire one.

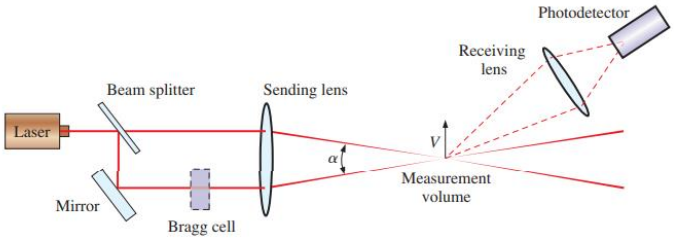

Figure **2-5**: A dual beam LDA system [16].

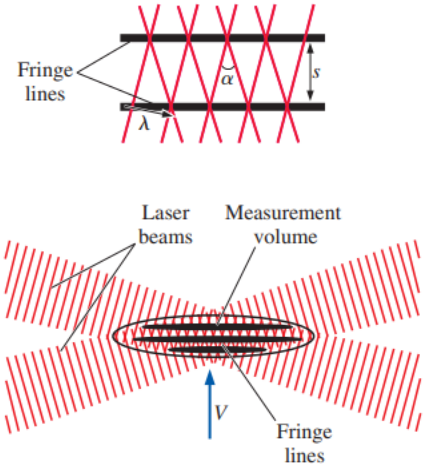

Figure **2-6**: Fringes formed from the interference at the intersection of two laser beams of an LDA system (bottom) and a close-up view of two fringes (top) [16].

Hot-Wire and Hot Film Anemometer

A hot-wire and hot film anemometer is an instrument used for measuring the velocity of fluids, consisting of two probes with a wire (film) stretched between them. These wires are typically made of tungsten, platinum, or platinum-iridium. When an electric current passes through this wire (film), it is heated up, shown in Figure 2-7. As the wire (film) is placed in the airflow, it cools down because of the relationship between resistance and temperature in metals. This change in wire (film) resistance can be used to measure the flow rate.

Hot-wire anemometry has two working modes: constant current and constant temperature type. In the constant current method, the current supply to the wire remains constant, and the temperature of the wire reduces based on the flow rate. The greater the flow rate, the more the temperature is reduced. Hence, when the temperature changes, the resistance of the hot wire changes, which is equal to the speed of the fluid flow. Whereas, in the constant temperature method, also known as the constant resistance method, the heating supply is continuously changed to replenish the loss of heat to the flow from the wire, to maintain a constant temperature. The greater the flow rate, the greater the current supplied to heat the wire, which can be used to determine the flow rate.

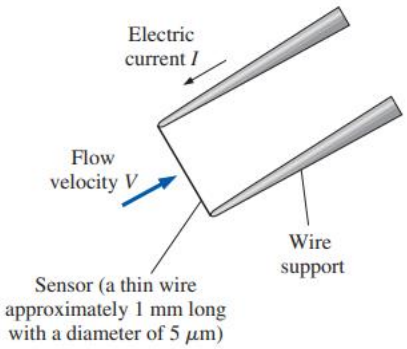

Figure **2-7**: The electrically heated sensor and its accompanying support structure form the essential components of a hot-wire probe [16].

Optical measurement Techniques

Particle Image Velocimetry

Measuring the fluid flow velocity by seeding the flow with small particles and illuminating the particles with a laser is the main underlying concept of Particle Image Velocimetry (PIV). High-speed cameras capture images of the particles and are post-processed to analyze the particle movement in every frame to calculate the velocity of the flow at various points in the flow field, as

shown in Figure 2-8. PIV is widely used in fluid dynamics research because it helps in understanding flow patterns, turbulence, and aerodynamic characteristics.

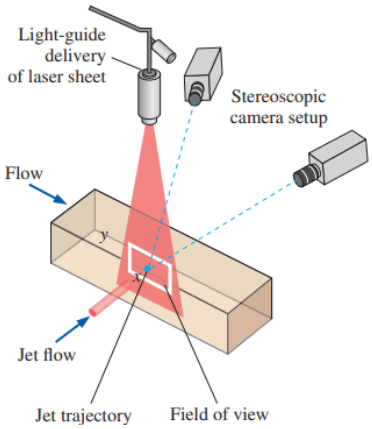

Figure **2-8**: A three-dimensional PIV system arranged to analyze the mixing of an air jet with cross-duct flow [16].

Schlieren Imaging

This optical technique works on the principle of light rays bending when they encounter a change in the density of a fluid. When light passes through a transparent medium with density variations, it undergoes a subtle change in direction due to the refractive index gradient, which cannot be observed directly. Changes in the light direction are magnified using a specialized optical setup. Based on the results this method produces, it is useful for observing density gradients and phenomena such as shock waves, thermal convection, and flow disturbances.

Flow Visualization Techniques

In fluid dynamics, making the fluid flow patterns visible in order to analyze their qualitative and quantitative characteristics. Flow visualization is classified and approached as: *Direct flow visualization* – techniques simplify flow data into easy visuals, like arrows or colored areas, showing flow direction and speed at a glance. *Dense, texture-based flow visualization* – adjusting and correlating texture values with the flow direction, it shows where the flow is moving.

Geometric flow visualization – integration to analyze flow data over time, creating geometric objects like streamlines, streaklines, and pathlines, which indicate flow behavior. *Feature-based flow visualization* – this approach first extracts key features from the flow data before visualization, it focuses on these extracted features, making visualization more efficient, especially for large or time-dependent datasets [28].

Flow visualization techniques used in wind tunnel testing are chosen based on the user requirements and work on different principles. Some of the commonly spoken visualizations are smoke, tufts, laser sheet, surface oil flow, and Holographic interferometry.

Smoke Flow Visualization

Smoke or aerosol particles are introduced into a fluid flow, creating visible traces that follow the movement of the flow. The flow patterns are visualized and analyzed by observing how the smoke disperses or moves within the flow. This method is particularly useful in wind tunnel experiments and atmospheric studies since it helps understand the behavior of airflow around objects or within natural environments.

Surface Oil Flow Visualization

This method involves applying a thin layer of oil or paint onto a surface exposed to the flow. As the fluid flows over the surface, it interacts with the pain or oil to create a visible pattern indicating flow characteristics such as separation points and boundary layer behavior. Common applications of this technique in aerodynamics and hydrodynamics to improve the design and performance of aircraft and ship hulls.

Chapter 3

Flow Quality Observations in an Additively Manufactured Wind Tunnel

Wind Tunnel Requirements for the Experiment

Low-speed, compact, easily configurable, additively manufactured small-footprint wind tunnels offer promising capabilities and can significantly enhance the assessment of flow performance in academic research. Based on the available space, application requirements, and non-complexity involved due to the involvement of a minimal number of parts, a small footprint open circuit wind tunnel of 12 in x 12 in x 3 ft in length with a mean velocity of 4-5 m/s was additively manufactured at a very low cost, as described by Wang et al. [9]. Based on these requirements, the wind tunnel was designed to comprise of 7 main parts: Bellmouth, Contraction, Louvre, Test Section, Blower Attachment, Diffuser, and Axial Fan, as shown in Figure 3-1.

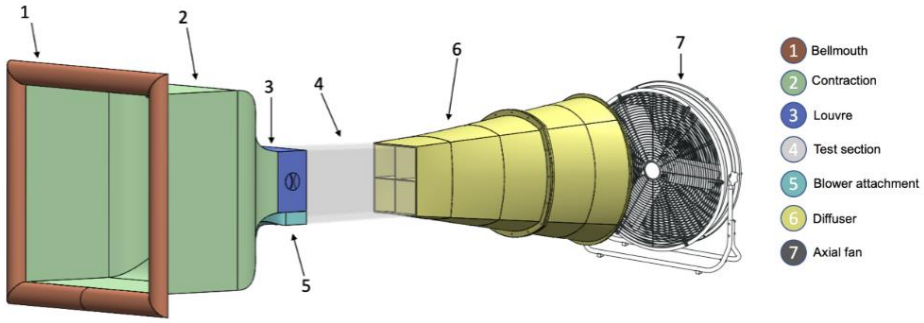

Figure **3-1**: Additively manufactured open circuit wind tunnel used for the experiments conducted in this thesis, with CAD model and part description [9].

The contraction section has a bell mouth at its inlet to help streamline the flow, which further leads to a settling chamber equipped with honeycombs that act as flow straighteners, and finally to a converging nozzle. A contraction ratio of 10.2:1 and a length of 18 in was chosen after careful evaluation. Since this wind tunnel was originally designed for reconfigurability, its main focus was investigating how much airflow is needed to lift metallic powders off the 3D printing

surface in techniques like Powder Bed Fusion (PBF). Hence, to replicate the wall jet created within a 3D printer, a secondary air source – a 6.4 HP blower was attached to the test section inlet. Right above the blower, a flow controller called louvre is accommodated to vary the flow entering the test section. This 6-inch section can be replaced with other flow conditioning devices or removed completely based on the requirements. Regulating the test section dimensions affects the overall wind tunnel's length. Hence, arrived on a 12 x 36 inches test section size, facilitated with the bottom controlled by a hydraulic build plate. The downstream end of the test section extends to a 48-inch diffuser with an unusually large 8.9 degrees expansion angle, due to space constraints. Due to this, a potential disruption in the airflow arises which can be controlled by dividing the diffuser into 4 chambers. One noticeable point is the effortless shift from rectangular to circular cross-section to house an axial fan at the latter end. The axial fan, located downstream, sucks air from the contraction through the diffuser and recirculates it back to the contraction. To control this fan driven wind tunnel effectively, a variable speed controller is used. This controller allows us to adjust the fan's speed over a wide range, and flexibility to conduct tests at different airflow conditions.

Experimental Results Obtained from the 3D Printed Wind Tunnel

Airflow quality was assessed by a 2.5 psi DSA3217 Scanivalve pressure scanner connected to an L-shaped pitot-static probe. Two locations defined at 2 and 17 inches downstream of the test section inlet were chosen to take multiple pressure readings at 5 points in the x direction and 14 y direction heights, to determine the velocity profile as seen in Figure 3-2. A well-functioning wind tunnel as shown in Figure 3-3 [29], and in this case, x =1^{st} and 5^{th} to show a similar trend, 2^{nd} and 4^{th} to follow the same. In contrast, the velocity profile at both locations 1 and 2 exhibited a trend where x =1^{st} and 2^{nd} had comparably lower magnitude than 5^{th} and 4^{th} points indicating a clear asymmetry in the flow, as indicated in Figure 3-3 [9].

Further, the turbulence intensity profiles were analyzed at these 2 locations, which showed that the lower boundary layers had the highest turbulence levels, after which there is a stability phase and the final rise in the turbulence due to the boundary layer effect at the top. One noteworthy observation is the turbulence values farther from the boundary layers (stability phase) are below 5% and 2.5% for locations 1 and 2 respectively.

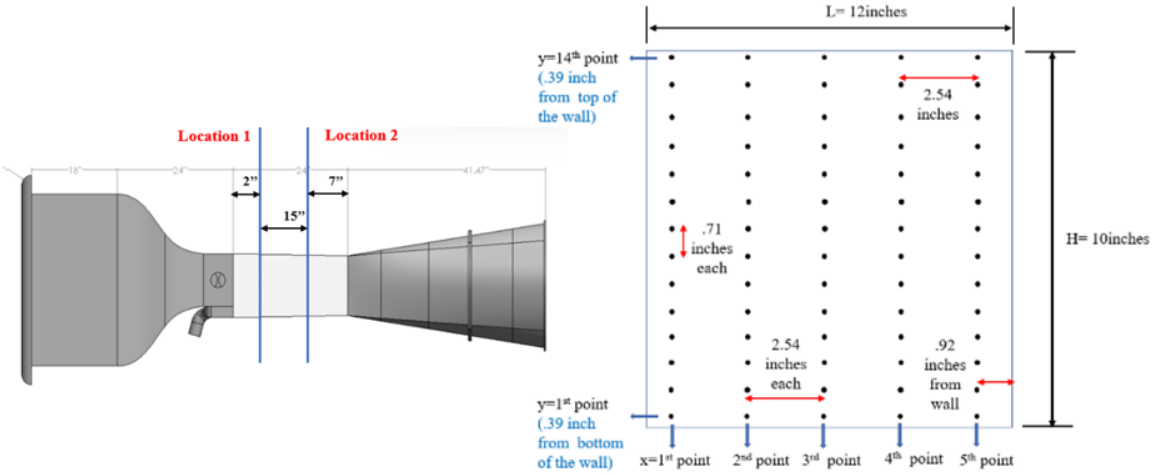

Figure **3-2**: Location and number of points where the pressure measurements were recorded from which the velocity profile was generated, along the x and y directions. [9].

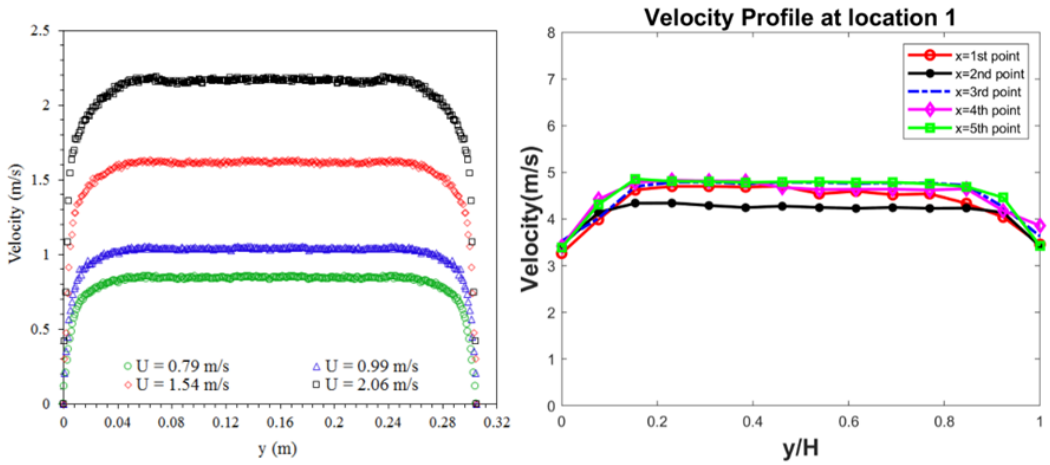

Figure **3-3**: Left: velocity profile of a well-functioning wind tunnel from [29], and Right: asymmetric velocity profile obtained from [9].

Gap/Challenges Observed from Testing

Producing velocities up to 5 m/s with a turbulence intensity of less than 2% along with keeping the cost minimal was the goal of this project. After experimental characterization of the wind tunnel, it showed results deviating from the expected quality flow. The key issue observed was the asymmetries involved with the velocity profiles and turbulence intensity levels resulting in slight asymmetry in the incoming flow and turbulence levels in the test section higher than planned.

One reason for this possible discrepancy is the 3D printed parts of the tunnel and the test section are attached by sealing it with rubber gaskets, which caused discrepancies in the symmetry of the tunnel. A misaligned tunnel produces irregular flow due to the airflow being disturbed by the geometry and alignment of the wind tunnel. Another reason could be due to the gaps between different sections of the wind tunnel possibly while joining the 3D printed parts with each other and while joining the acrylic test sections. These gaps create flow disturbance and loss of pressure in the wind tunnel leading to inaccurate measurements.

The most important factor affected due to asymmetry and gaps in the wind tunnel is the boundary layer effect. Disruptions in the smooth airflow affect the boundary layer to cause uneven flow profile, premature separation, delayed reattachment, and thicker or thinner boundary layer.

Chapter 4

Improvements Towards Achieving Quality Flow in the Wind Tunnel

Suggested Modifications

Tackling the asymmetries observed proves to be challenging when a conclusion on the root cause cannot be narrowed down. In Wang et al. [9], certain structural changes were suggested by the current work: addition of a set of flanges that connects all the wind tunnel parts; realignment of the tunnel to ensure straightness of flow; a slight widening of the test section to generate a smoother flow and counteract the effects of displacement; and fine-tuning the flow conditioning in the settling chamber to reduce turbulence intensity. Incorporating these ideas was hypothesized to enhance uniformity in the flow, turbulence, and control the flow as it progresses into the tunnel.

Structural Improvements

This thesis focuses on implementing structural additions such as connector flanges at the identified sections of the tunnel. Noticeable problem locations were at the connecting areas of the inlet and outlet of the test sections. Hence, two pairs of connecting parts were to be designed to overcome the gaps created between the diffuser – test section and blower – test section areas. It was later observed that in addition to these flanges, it was necessary to implement another pair of connectors for the louvre – contraction parts. All the three locations are indicated in the below Figure 4-1.

Several factors needed to be considered while designing the connectors: Precise design to snug fit without causing disruptions in the flow; Incorporating effective sealing mechanisms along with the flanges to ensure there is no leakage; Maintaining proper alignment of the flanges and the tunnel to avoid irregular flow; Considering easily accessible and maintainable flanges which eases instrumentation and inspection purposes.

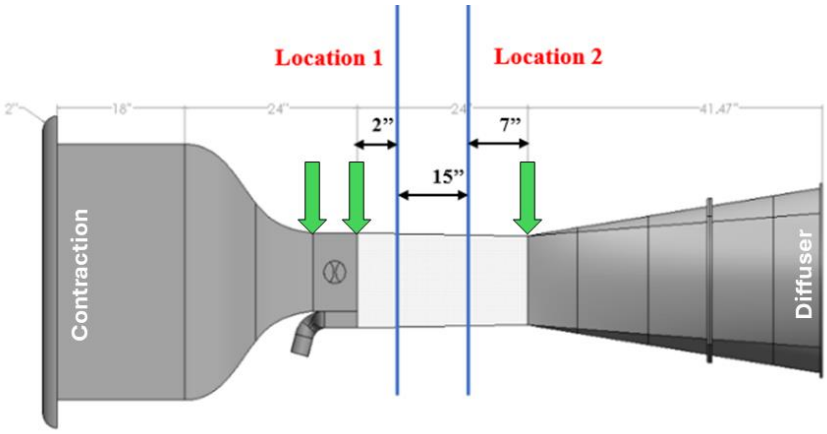

Figure **4-1**: Location of the flanges are indicated by the green arrows [9].

Design Requirements for the Flanges

From previous literature [21], [30], [31], [32], flange incorporation into the tunnel will add to the structural integrity, enhance aerodynamic performance, and flow distribution reduction. The final design of the flanges was to design the flanges with the same circumferential shape as the part it would be attached to. Once this flange design as finalized, it was determined that the tunnel needed six flanges, with two flanges mating at each location, resulting in three pairs of mating flanges between different sections to address the gap and tackle the asymmetric airflow. The first step towards achieving this is designing the flanges dimensionally accurate to fit the tunnel parts precisely while keeping the space constraints in mind. The most important factor to consider is the shape of the flanges while making sure it is designed for manufacturing while abiding by the design requirements. One noteworthy observation is that the flanges are to be fitted only on the top and the sides, not on the bottom because it would restrict the accessibility of the build plate. Another observation was the shape of the diffuser and contraction sections were of varying cross-sectional area rather than a simple square or rectangular area section like the test section. Initially, the basic C-shaped flanges were modeled on SOLIDWORKS which would fit the inlet and outlet of the test-

section and on both sides of the louvre. Finally, the complicated diffuser and contraction side flanges were designed. The final design for all the flanges are shown in Figures 4-2 and 4-3.

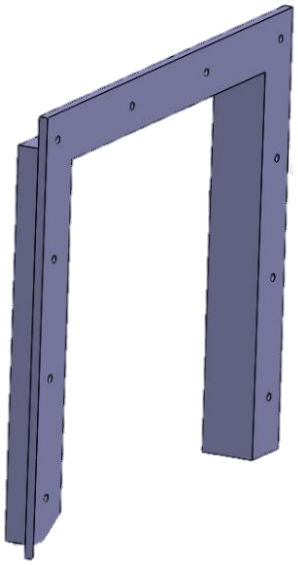

Figure **4-2**: Final design of the flange shape used for the wind tunnel, modeled on SOLIDWORKS.

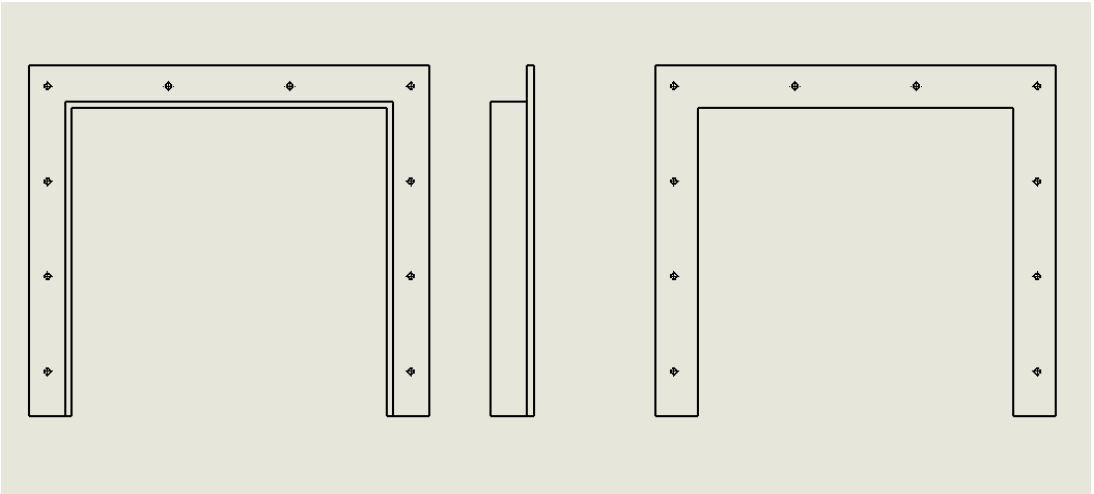

Figure **4-3**: Orthographic projection views of the basic flange design modeled for the Wind Tunnel.

Location of the Flanges and Dimensions

Asymmetries and gaps arise due to the different materials used in the manufacture of the wind tunnel. To be precise, the 3D printed parts and acrylic test section had irregularities to form a smooth aligned fit. Even after an additional layer of rubber sealants and adhesives were used to fill these gaps, an asymmetry in the velocity profiles were observed in wind tunnel as described in Chapter 3. Hence, the Diffuser – Test section and Blower/ Louvre – Test section areas were identified with asymmetries and gaps, hence the need for connecting flanges at these locations. It was later identified that the Blower/ Louvre – Contraction side required another set of flanges to be added due to the gap created between these two parts.

During the flange design, it was observed that the cross-section of the diffuser smoothly transitions from the rectangular profile of the test section to a circular profile, which meant the flange needs to be designed following the diffuser cross-section. Similarly, the contraction chamber transitions from a smaller to larger area. Due to this, the flange design needs to adhere to the changing area of the contraction.

Diffuser – Test section flange

Firstly, the basic Test-section side flange was designed to snugly fit the 12.75 in x 13 in Test-section. After which, the Diffuser flange to fit the 12 in x 12 in Diffuser was designed. Both these flanges are 14.5 in length x 16.5 in width, with equally spaced holes of 0.25 in diameter as shown in Figure 4-4. These flanges were then fitted onto the diffuser and test section to ensure they abide by the dimensions of the parts, as shown in Figures 4-5 and 4-6.

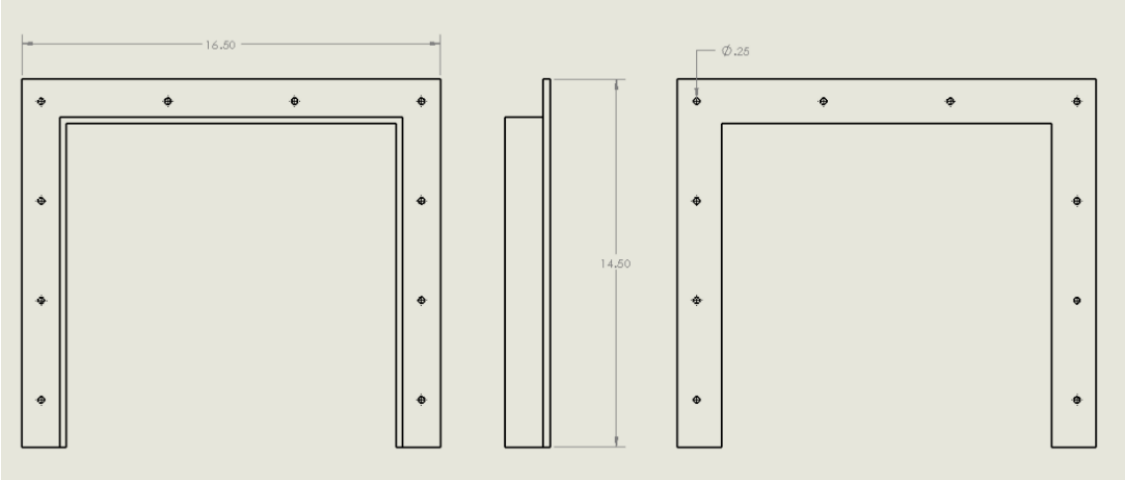

Figure **4-4**: Orthographic projection views of the Diffuser and Test section side flanges marked with basic dimensions.

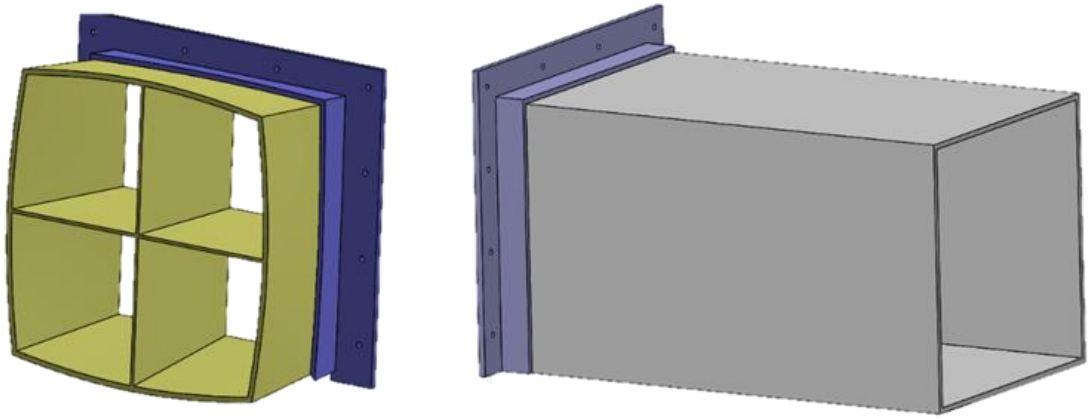

Figure **4-5**: Left picture shows the 3D model of the snug fitted Diffuser flange (only a part of the diffuser is shown for easier interpretation). The right picture shows a snugly fitted model of the Test section side flange.

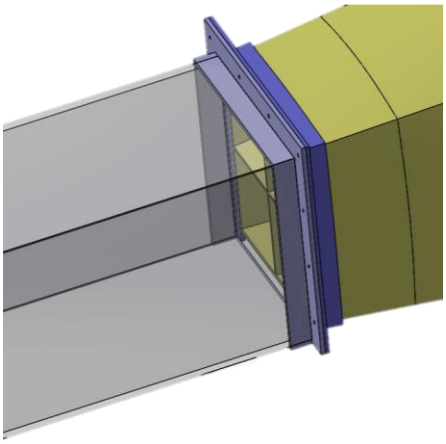

Figure **4-6**: Assembled Test section – Diffuser flanges (Only a part of the Diffuser and Test section are shown for ease of view).

Blower/ Louvre – Test section flange

After the diffuser side flanges were designed, the other side of the Test section side flange was designed to snugly fit the 12.75 in x 13 in Test section. After that, the Louvre flange was designed to fit the 13 in x 12.75 in louvre and blower. The pair of flanges were designed with a 14.75 in length x 18 in width, with equally spaced holes of 0.25 in diameter as shown in Figure 4-7. These flanges were then fitted onto the Blower/ Louvre and test section side to ensure they abide by the dimensions of the parts, as shown in Figures 4-8 and 4-9.

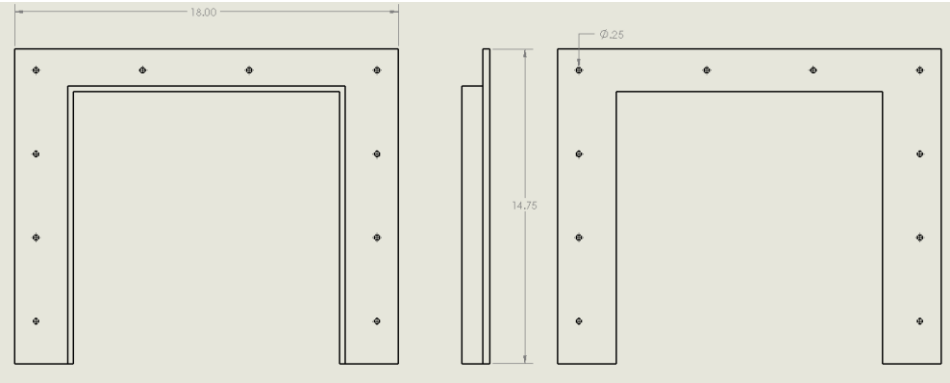

Figure **4-7:** Orthographic projection views of the Blower/ Louvre and Test section side flanges marked with basic dimensions.

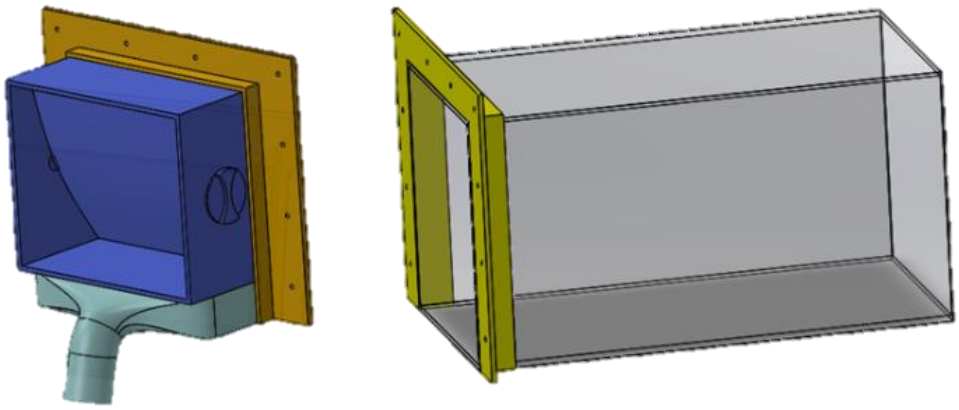

Figure **4-8**: Image on the left and right show the 3D model of a snug fitted Blower/ Louvre and Test section side flanges respectively.

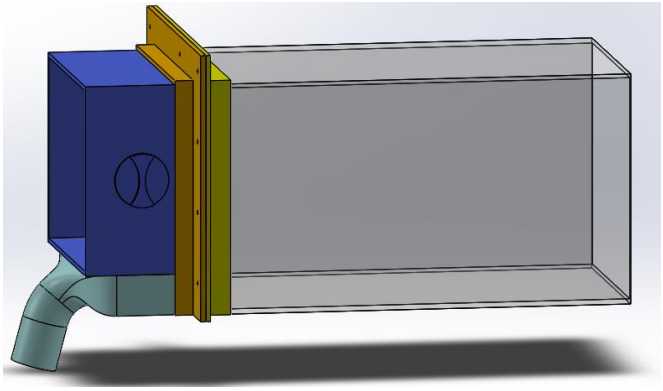

Figure **4-9**: Assembled Blower/ Louvre – Test section flanges.

Blower/ Louvre – Contraction flange

Lastly, after identifying a gap around the contact areas of the Louvre and contraction, it was determined that a pair of flanges needed to be designed to seal the gaps. Hence, one set of flanges was designed to fit the 10.5 in x 13 in Louvre and 10 in x 12.5 in Contraction. These flanges were designed with an 11.5 in length x 14.5 in width having equally spaced holes of 0.25 in diameter as shown in Figure 4-10 and are assembled onto the Blower/ Louvre and Contraction side to ensure they abide by the dimensions of the parts, as shown in Figure 4-11.

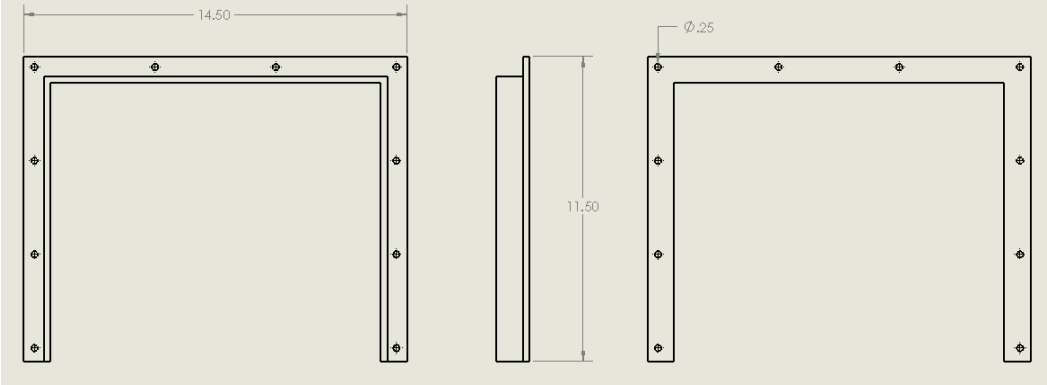

Figure **4-10**: Orthographic projection views of the Blower/ Louvre and Contraction side flanges marked with basic dimensions.

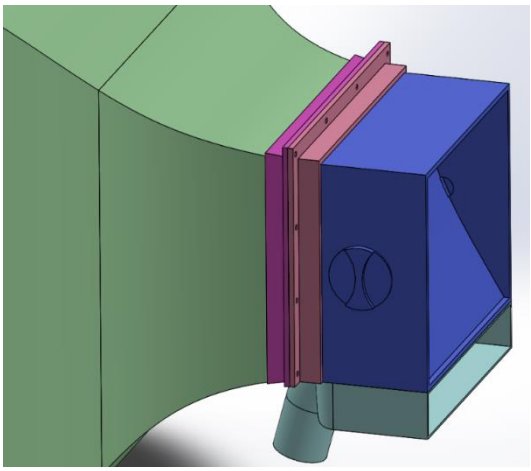

Figure **4-11**: Assembled Blower/ Louvre – Contraction flanges (Only a part of the Contraction is shown for ease of view).

Flange Placement in the Wind Tunnel

All three pairs of flanges were designed to be attached to the ends of each section which would increase the wind tunnel's length significantly. Keeping in mind the space constraints, the best way to interface parts by minimizing the gap is through snug fit. Hence, the flanges were designed to have a tight fit and would be placed over the components rather than connecting to the ends of the tunnel parts as shown in Figure 4-12 and 4-13.

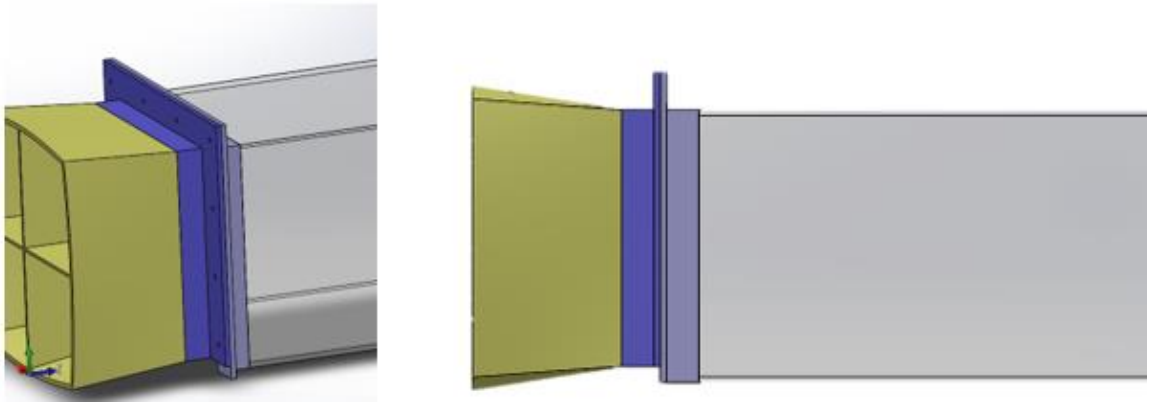

Figure **4-12**: Initial flange design, which gets attached to the edges of the sections of the Wind Tunnel increasing its length.

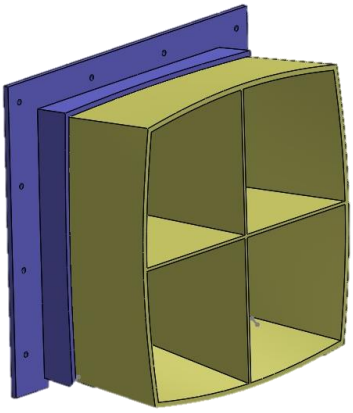

Figure **4-13**: The finalized flange design chosen to snug fit over the parts of the Wind Tunnel to ensure better sealing and gap closure.

Followed by the 3D modeling of the flanges, it is necessary to check if they adhere to the dimensional specifications and if they fit precisely on the wind tunnel. This was done by creating an assembly of the wind tunnel integrated with these 6 flanges. The assembled model of the wind tunnel showed dimensionally adhering snugly fit flanges as shown in Figure 4-14, with the parts of the wind tunnel named in Table 4-1.

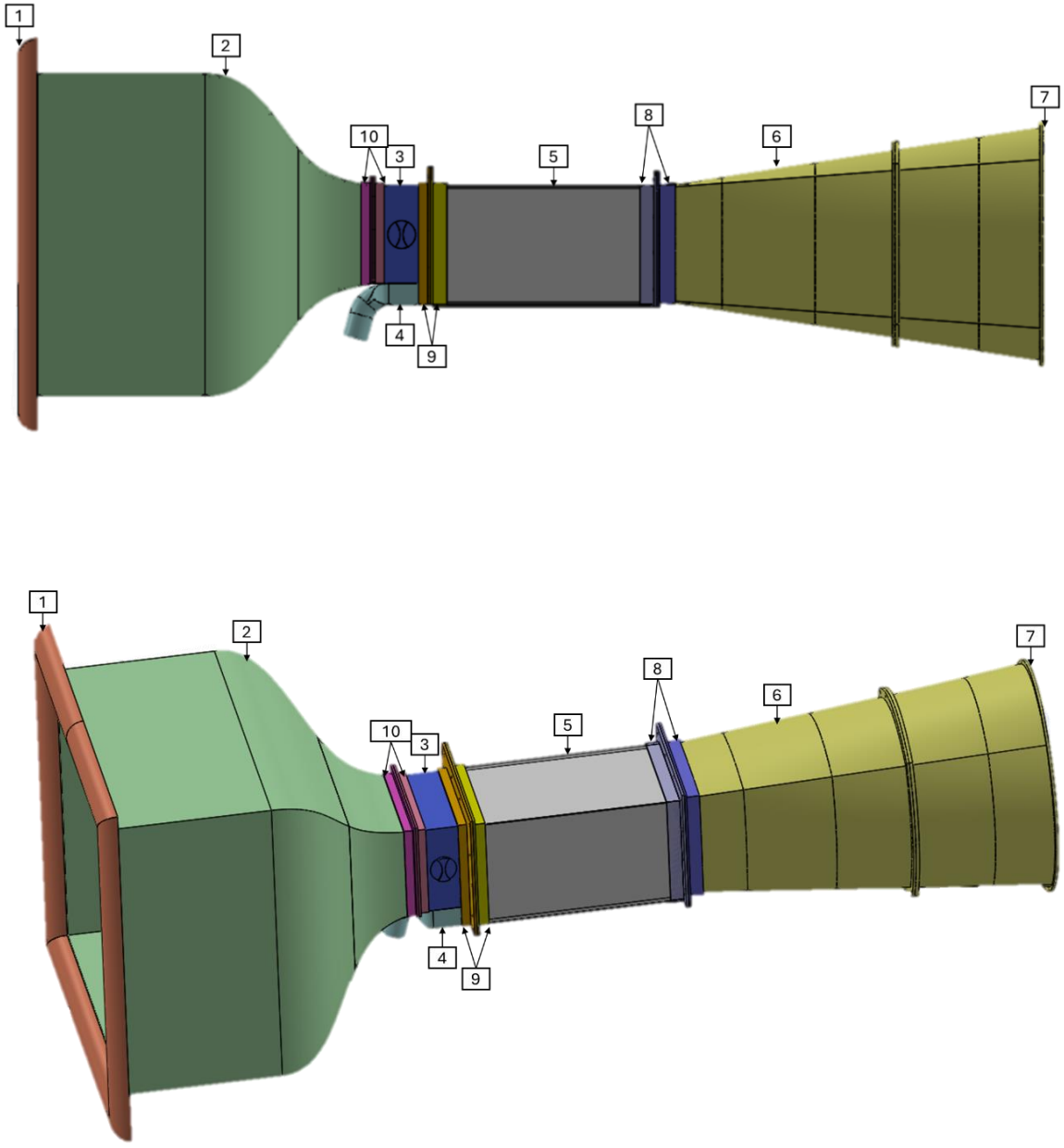

Figure **4-14**: Top view (Top) and orthographic view (down) of the assembled wind tunnel with flanges (Legend table given below).

Table **4-1**: Part description of the Wind Tunnel with its associated legend.

Legend	Wind Tunnel Part Name
1	Bellmouth
2	Contraction
3	Louvre
4	Blower
5	Test-section
6	Diffuser
7	Axial Fan
8	Diffuser – Test-section flange
9	Blower/ Louvre – Test-section flange
10	Blower/ Louvre – Contraction flange

Additively Manufactured Flanges

After assessing the fit of the flanges, the next step is to 3D print them using the guidelines of Design for Additive Manufacturing (DfAM) [33]. The printer used was a LulzBot TAZ Workhorse with a 2.85 mm diameter nozzle using PLA (Polylactic Acid). material for printing, as shown in Figure 4-15. PLA is a popular filament material used in 3D printing due to its biodegradability, ease of use, and wide availability [34]. The Cura LulzBot software was used as an interface for printing the parts, which had the options of scaling, positioning, and orienting parts, which helped preview before the actual part was printed, seen in Figures 4-16 and 4-17. The print bed is heated to 60^0C and the nozzle to $215 - 235^0C$, as per the recommendation from the 'TAZ_Workhorse_Manual', to ensure the right temperatures are reached.

Due to the restrictions of the size of the flanges and complicated shape [35], the optimal approach to 3D printing was to segment each flange into four parts such that it fits the printer bed.

This method of dividing a single file into multiple parts to best fit the 3D print volume is called slicing. Slicing resulted in 4 subparts of each flange, resulting in 24 3D-printed parts.

Finally, the 3D printed parts are held together using Weld16 glue and then a wood burner is used to melt the PLA to fill the gaps and material imperfections of the parts. Each of the 4 subparts are held together using this technique to produce a complete flange shown in Figure 4-18.

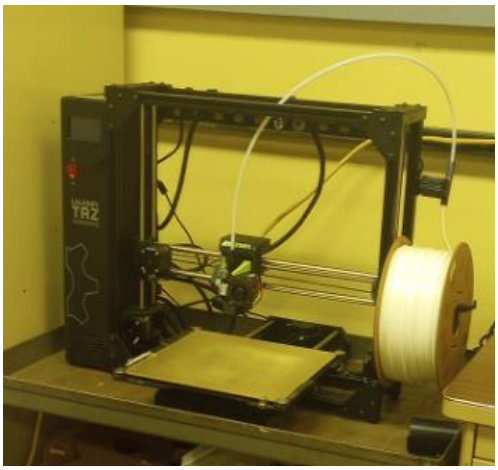

Figure **4-15**: LulzBot TAZ Workhorse 3D printer used for flange production.

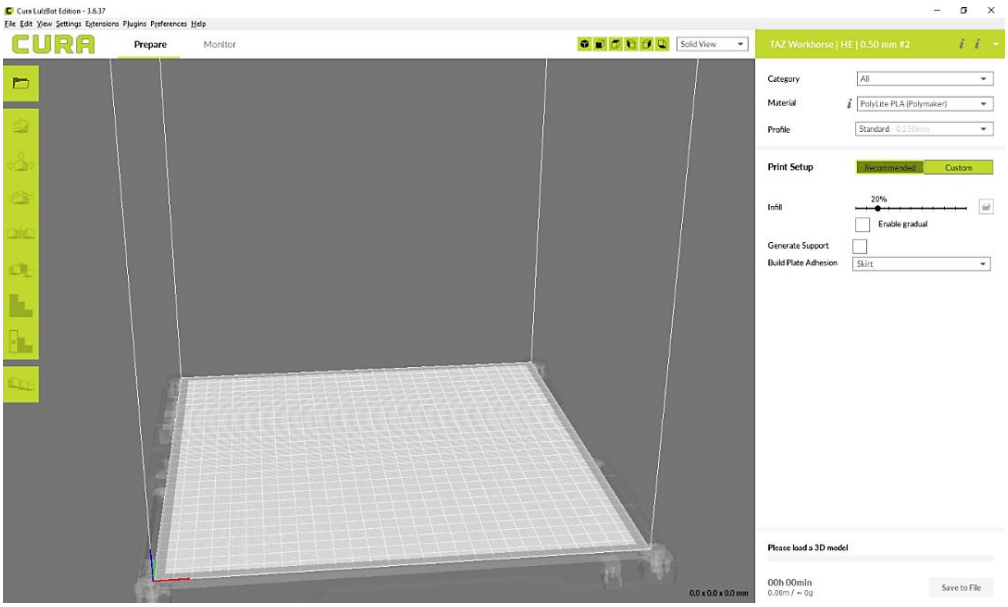

Figure **4-16**: Cura LulzBot software used for 3D printing the flanges, showing the print bed where the CAD model will be placed.

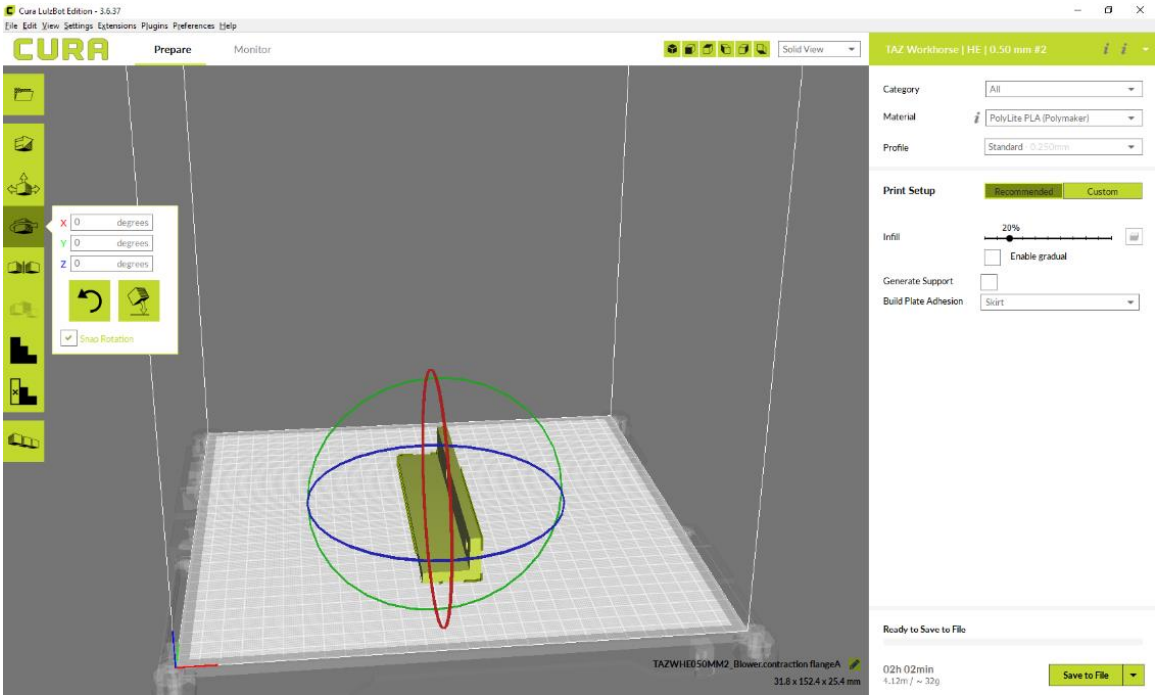

Figure **4-17**: SolidWorks model of the flange placed on the print bed in the Cura LulzBot software with the freedom of rotating the part to achieve the desired orientation.

Figure **4-18**: A 3D printed fully joined flange.

Flange Assembly and Wind Tunnel Alignment

The necessary flange parts were organized according to their location, and four parts were glued together to form one full flange. This process resulted in pairs of six full flanges. First, the Diffuser – Test-section flange was placed onto the wind tunnel to ensure a snug fit and check if the holes were aligned with their corresponding mating part. Subsequently, the Blower/ Louvre – Test-section flanges and Blower/ Louvre – Contraction flanges were fitted to verify the same as shown in Figure 4-19.

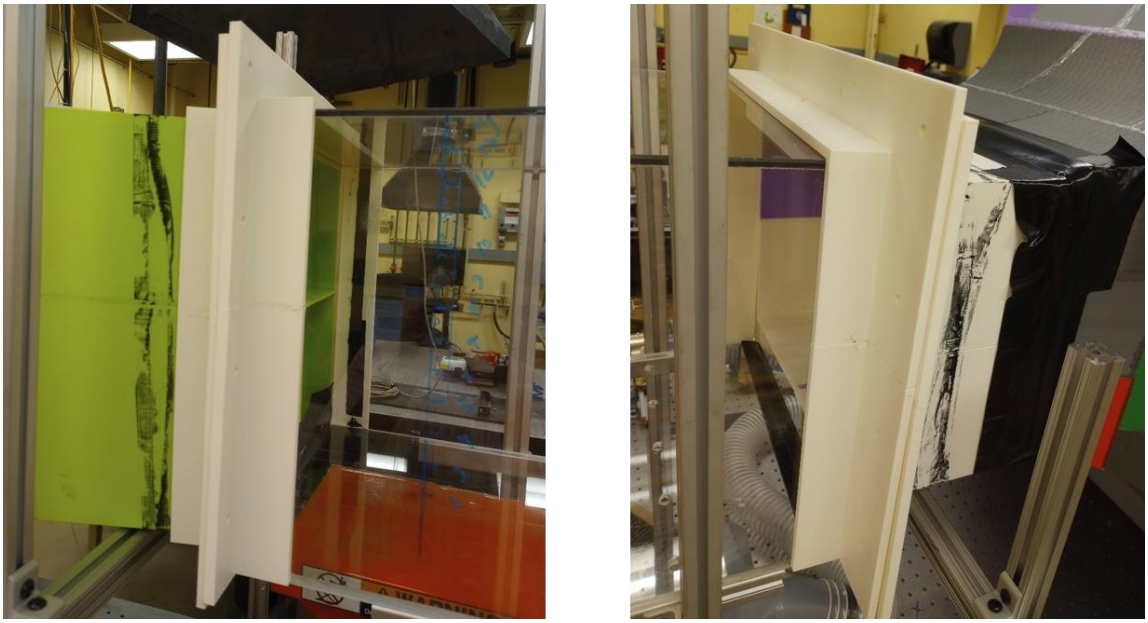

Figure **4-19**: Diffuser – Test section flanges (Left) and Blower/ Louvre – Test section flanges (right) assembled onto the Wind Tunnel.

The next step involved aligning the wind tunnel with the flanges. The wind tunnel was visually aligned, and a Tapedo leveler was used to ensure it appeared straight and level. Several pressure measurements were then recorded to calculate the velocity and verify the accuracy of the wind tunnel readings. This process ensured that the tunnel was precisely angled as required and ready for temporary fastening.

All three sets of flanges were temporarily assembled onto the wind tunnel using adhesive tape as shown in Figure 4-20. It was ensured that the wind tunnel was stable and securely fixed, and pressure readings were recorded at different locations, including those close to the side test section walls, at the lowest and highest heights. These readings produced a velocity profile that mimicked that of a well-functioning wind tunnel [29]. A well-functioning wind tunnel produces a uniform velocity profile with low turbulence intensity (Figure 4-21), stable flow conditions, and accurately simulates real-world conditions while providing precise and reliable measurement data. Specifically, the velocity profile should be flat and uniform across the central region of the test section. Consequently, the final step involves permanently fixing the flanges onto each part of the wind tunnel and joining each pair of flanges by fastening the bolts, ensuring no gaps existed between them.

Figure **4-20**: Flanges assembled onto the Wind Tunnel with adhesive tape.

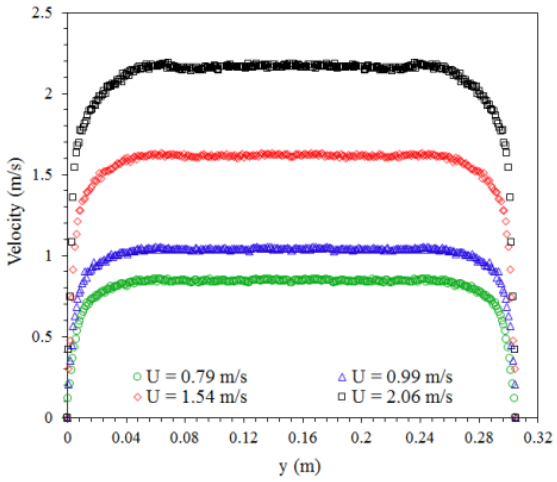

Figure **4-21**: Velocity profiles at wind tunnel outlet for different blower speeds from [29].

Chapter 5

Wind Tunnel Instrumentation and Testing

Test Techniques

To assess the flow quality through the tunnel, it is necessary to obtain the velocity profiles and turbulence intensity at different parts of the tunnel. This is done by measuring the pressure in the tunnel using a pitot-static probe connected to a 16-channel 2.5 psi DSA3217 Scanivalve pressure scanner and then converting these pressure readings to velocity.

A hydraulic-operated adjustable build plate with 5 holes spaced 2.54 inches apart in the x direction along the width of the plate is used to take multiple pressure values using a pitot-static pressure probe. Pressure measurements are noted across two locations: test-section inlet and outlet (Locations 1 & 2), at five different x locations and y along multiple heights of the test-section as in Figure 5-1 and Figure 5-2.

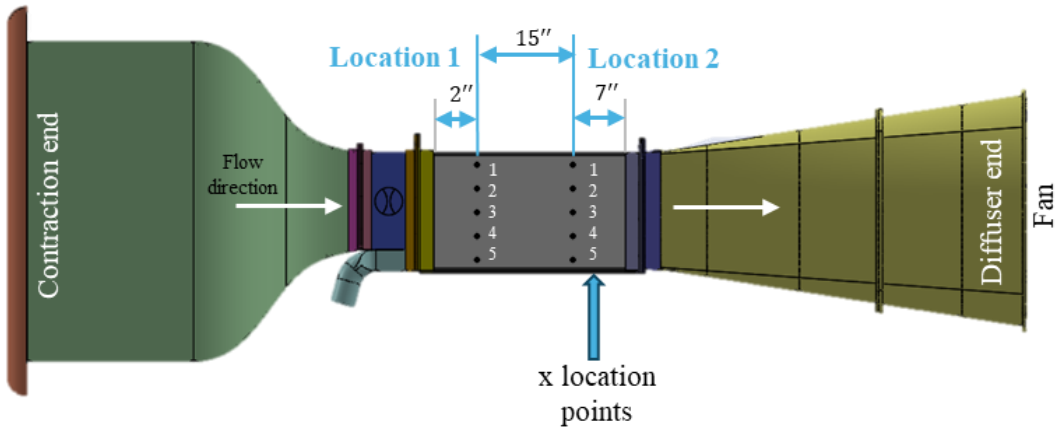

Figure **5-1:** Choosing the two locations, one on the diffuser end and the other on the contraction end to take pressure measurements at. Also marked are the order of the five x-location holes where readings are recorded.

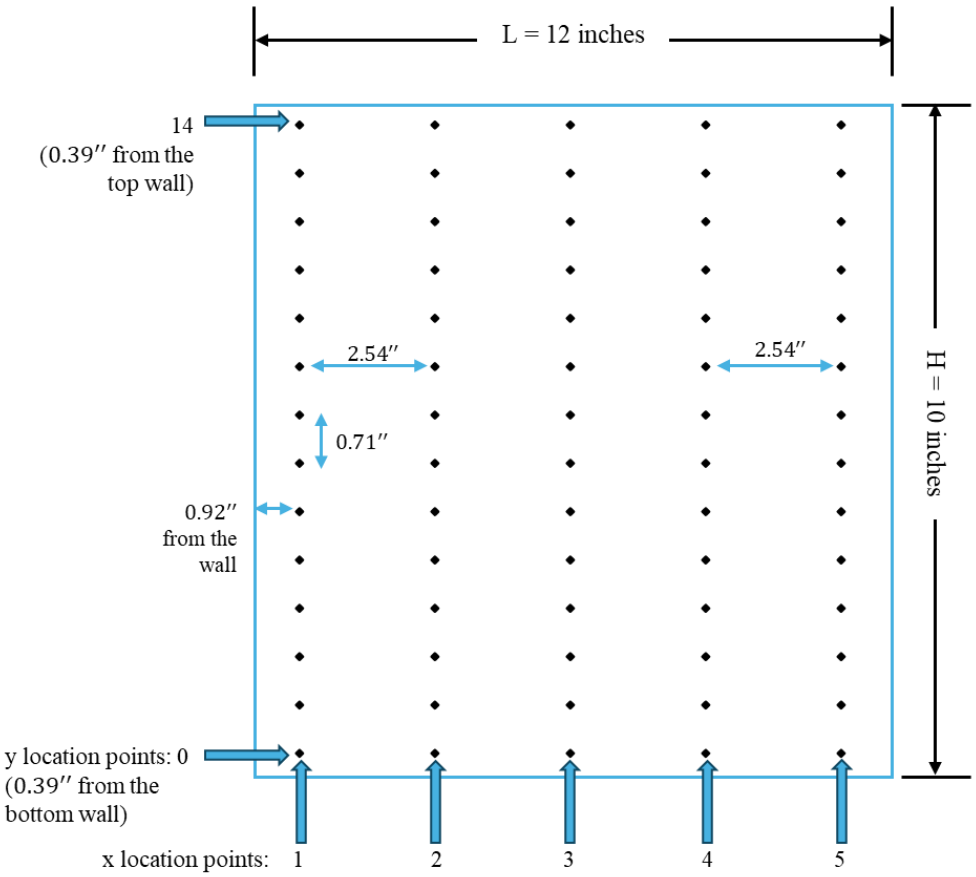

Figure **5-2:** Location and number of pressure measurements taken in x and y locations of the test section of the Wind Tunnel.

Test for Repeatability

Testing for a test setup capability to reproduce the same results consistently when repeated multiple times under the same test conditions is called repeatability testing. To check if the wind tunnel produced uniform readings constantly, the velocity readings at the same point were measured four times for different time intervals. It was noted that the velocity readings were consistently the same with a very small deviation from each other, proving that the wind tunnel is in good working order to produce accurate results indicated in Table 5-1.

Particularly, velocity measurements at all the five x-locations with different y-direction heights were measured and plotted with an error graph as shown in Figure 5-3. All the locations in the graph are independent of each other and the error bars are indicated in the same graph for conciseness. The graph indicates the mean (blue bubbles) and vertical error bars, i.e., standard deviation, SD (black lines), on each point illustrates the range of variability or uncertainty in the measurements, with longer error bars indicating higher variability and shorter ones indicating more precision. Overall, all the locations have a mean range of 4.501-4.545 and SD between 0.011-0.034, indicating repeatable results.

Table **5-1**: Repeatability test at locations x2 and x3 of the wind tunnel under the same testing conditions yields approximately constant velocity values.

No. of trails at x2, y9	Velocity (m/s)
1	4.476
2	4.475
3	4.459
4	4.414

No. of trails at x3, y10	Velocity (m/s)
1	4.403
2	4.523
3	4.505
4	4.497

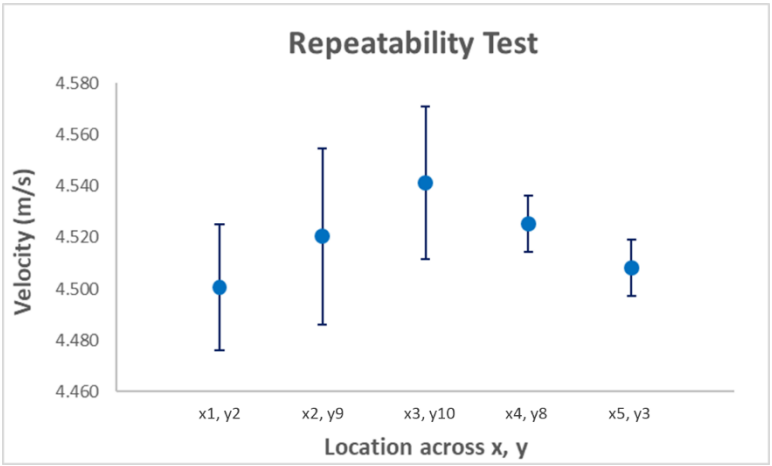

Figure **5-3**: Error bar graph indicating the repeatability of the velocities at different locations.

Determining the Standard Frame Rate and Time

Determining a suitable time interval to perform the experiment plays a crucial role in producing effective results in shorter time spans. A suitable frame rate needs to be chosen in a way that does not run lengthy experiments to yield the same result when they are run at shorter intervals of time. Hence an optimal time is determined by conducting multiple tests for different time periods, which is the same as changing the frame rate in the DSALink4 software. Multiple measurements were taken across various chosen frame rates of 100, 250, 500, 750, and 1000 which corresponds to 33, 83, 162, 249, and 322 seconds. Once the measurements were noted down and the velocities were calculated, the mean and Standard Deviation (SD) for each of these 5 frame rates was determined indicated in Table 5-2. By determining the SD, we can deduce the frame rate with the lowest SD was chosen as the ideal time period to perform the experiments as shown in Figure 5-4.

Moreover, the selection of 250 frames as having the lowest standard deviation (SD) indicates it provides the most consistent and precise data among the options considered. A low SD suggests that the data points are closely clustered around the mean, signifying minimal variability or dispersion in the measurements. In the context of frame rates, this means that at 250 frames, the intervals between consecutive frames are relatively consistent, resulting in more reliable and stable data. Higher frame rates have higher SD because measuring for longer, measure more instabilities in the flow. It is possible that increasing the frame rate too much could introduce additional sources of variability or noise that outweigh the benefits of capturing more data points. From the results obtained, it was observed that 250 frame rates had the lowest SD and hence the same was plugged into the Scanivalve software settings as shown in Figure 5-5.

Table **5-2**: Standard Deviation of each of the five chosen frame rates indicates that 250 frames are ideal to perform the experiment.

	X1,Y9	X2,Y9	X3, Y9	X4,Y9	X5,Y9			
# of frames collected	Velocity (m/s)					Mean	Standard deviation	Time (seconds)
100	4.335	4.359	4.466	4.433	4.343	4.387	0.059	33
250	4.359	4.343	4.411	4.429	4.425	4.394	0.040	80
500	4.355	4.366	4.368	4.177	4.423	4.338	0.094	162
750	4.358	4.374	4.368	4.094	4.417	4.322	0.129	249
1000	4.353	4.364	4.531	3.861	4.410	4.304	0.258	322

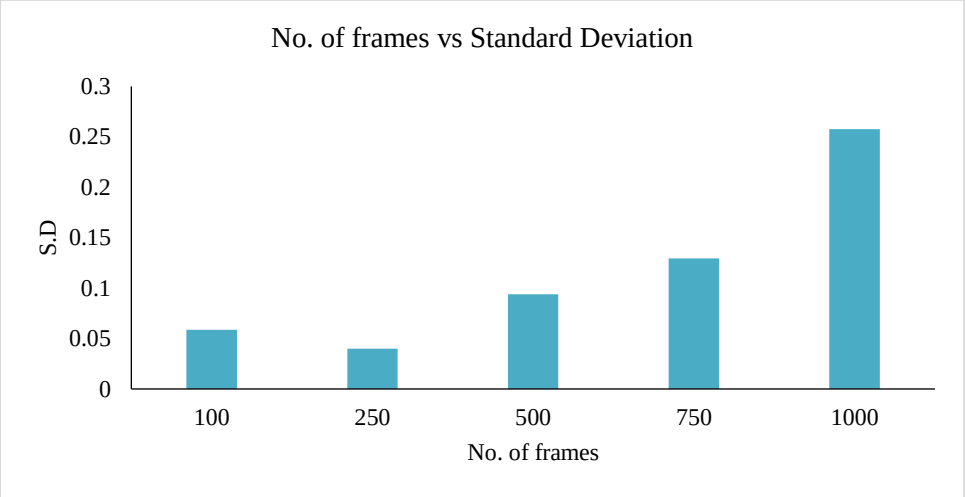

Figure **5-4**: Bar graph representing the Standard Deviations of different frame rates under consideration.

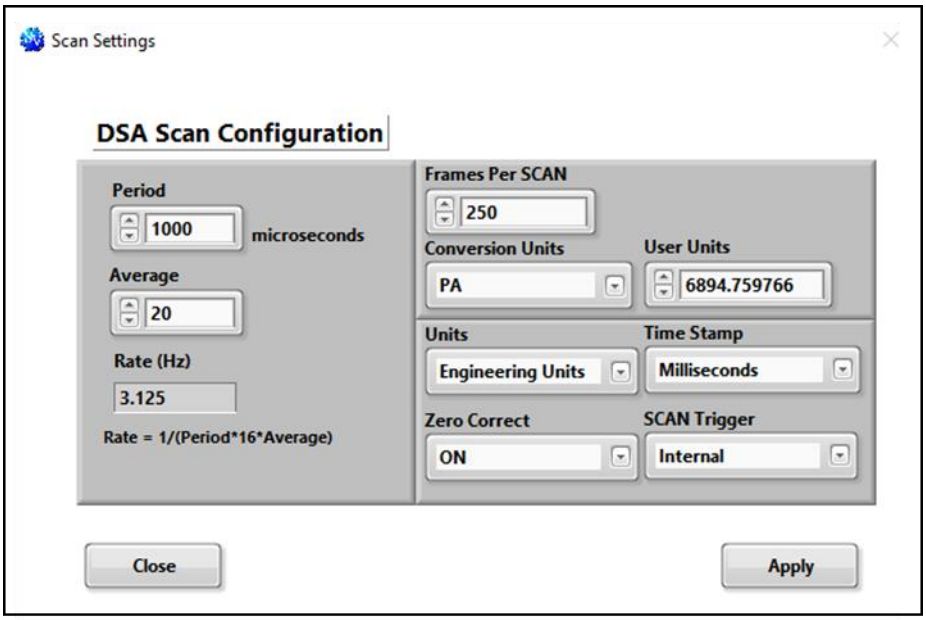

Figure **5-5**: Scan settings chosen for the DSA Scanivalve software used for the experiment using 250 frames.

Observations – Velocity Flow Measurement and Turbulence Intensity

Once the wind tunnel is set up with locations marked for measuring the pressure, the wind tunnel is turned on and left to run for some time before recording the pressure readings. This is done to make sure the tunnel is stabilized to yield accurate pressure values. The readings are taken along 5 locations on the x-axis distributed 2.54 inches apart equally, and 14 locations on the y-axis with increasing heights of 0.71 inches and 0.39 inches from the walls. Once the pressure scanner starts recording the readings for 250 frames, the pressure readings are converted to velocity readings using the formula: $p = {}^{1}/_{2}\,\rho v^2$, where p = total pressure, ρ = density of the fluid (air), and v = velocity of the fluid.

The velocity profile obtained at Location 1 from x = 1st to 5th points show almost constant velocity values between 4.4 – 4.6 m/s and lower velocity values at the top and bottom walls of the

test section due to the boundary layer effect as shown in Figure 5-6. To understand this effect, it is necessary to measure multiple velocity values at the boundary layer (i.e. points where the velocity starts decreasing) at the walls. Hence, seven extra points were added randomly to ensure a more accurate plot is obtained. Four points were added in between the 0^{th} and 3^{rd} point, and three points were added in between 12^{th} and 14^{th} points as shown in Figure 5-7.

The velocity values of the newly added points were recorded and added to the existing graph to obtain a more accurate velocity profile at both locations, and to better understand the boundary layer effect in wind tunnel operation.

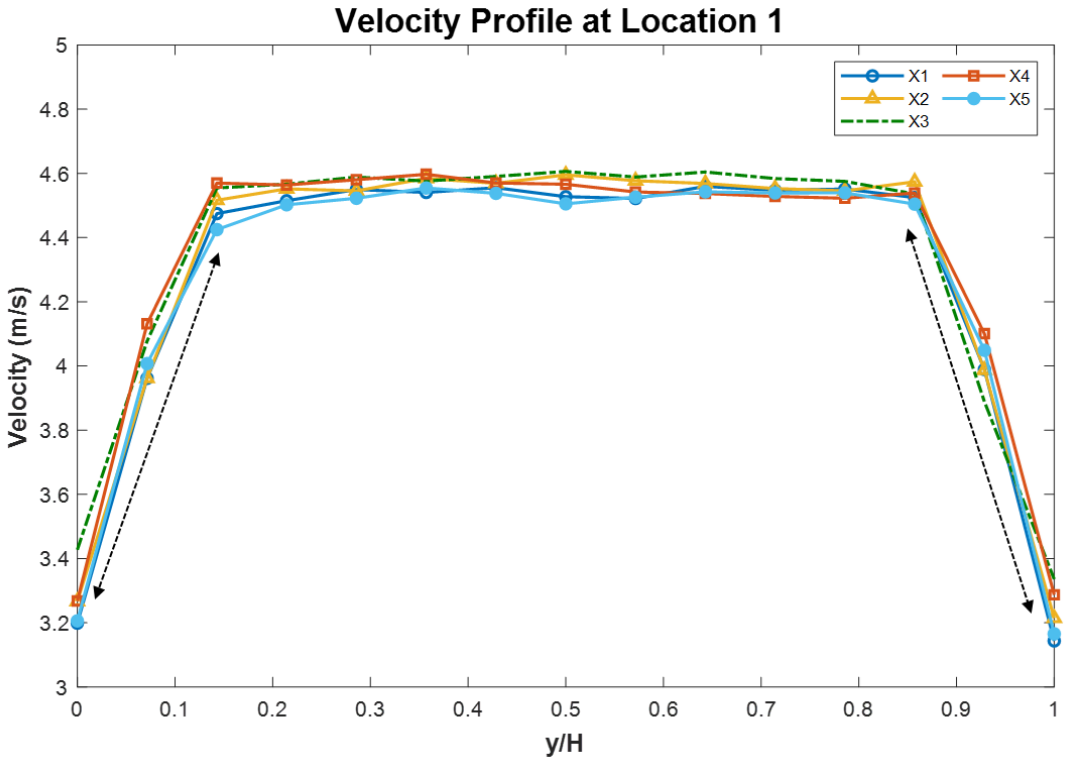

Figure **5-6**: Velocity Profile along 14 y-axis points at Location 1. Black dotted lines represent the range between which the new velocity values are to be measured.

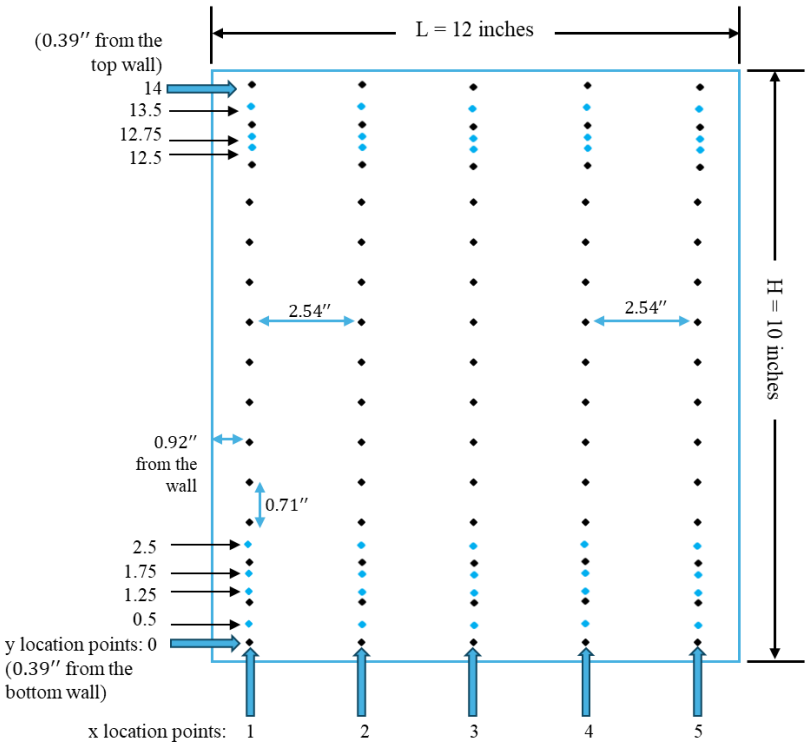

Figure **5-7:** Similar to Figure 5-2 with the location of the seven suggested points (in blue) added to record pressure measurements in y direction of the test section of the Wind Tunnel.

Velocity Profile at Location 1

Velocity measurements at Location 1 are presented in Figure 5-8 which resembles the velocity profile of an accurately functioning wind tunnel [29]. The reason for this conclusion is because of the similarity in magnitude of the velocity profiles at x = 1st and 5th points, along with 2nd and 4th points showing similar trends (Figures 5-8 and 5-9). Also, the velocity profiles at x = 3rd point is the highest with its velocity values being higher at the top and bottom walls when compared to the other points. Consequently, x = 2nd and 4th points lie right below it and lastly, x = 1st and 5th points are lower in magnitude due to the boundary layer effect (Figure 5-9). It is noteworthy to mention that the boundary layer has a thickness of under y/H = 0.15 and 0.1, as indicated by the measurements near the bottom and top walls respectively.

Velocity Profile at Location 2

Velocity Profile at Location 2 shows a similar trend as Location 1 and is presented in Figure 5-10 and 5-11. It is evident from the graphs that x = 3rd point has the highest velocity start and end points, followed by x = 2nd and 4th points. As the velocity values are recorded closer to the boundary layer, such as in x = 1st and 5th points, decreased velocity values are observed due to the boundary layer effect. Notably, the boundary layer has a thickness of under y/H = 0.15 and 0.18, near the bottom and top walls respectively, which are almost close to the Location 1 values.

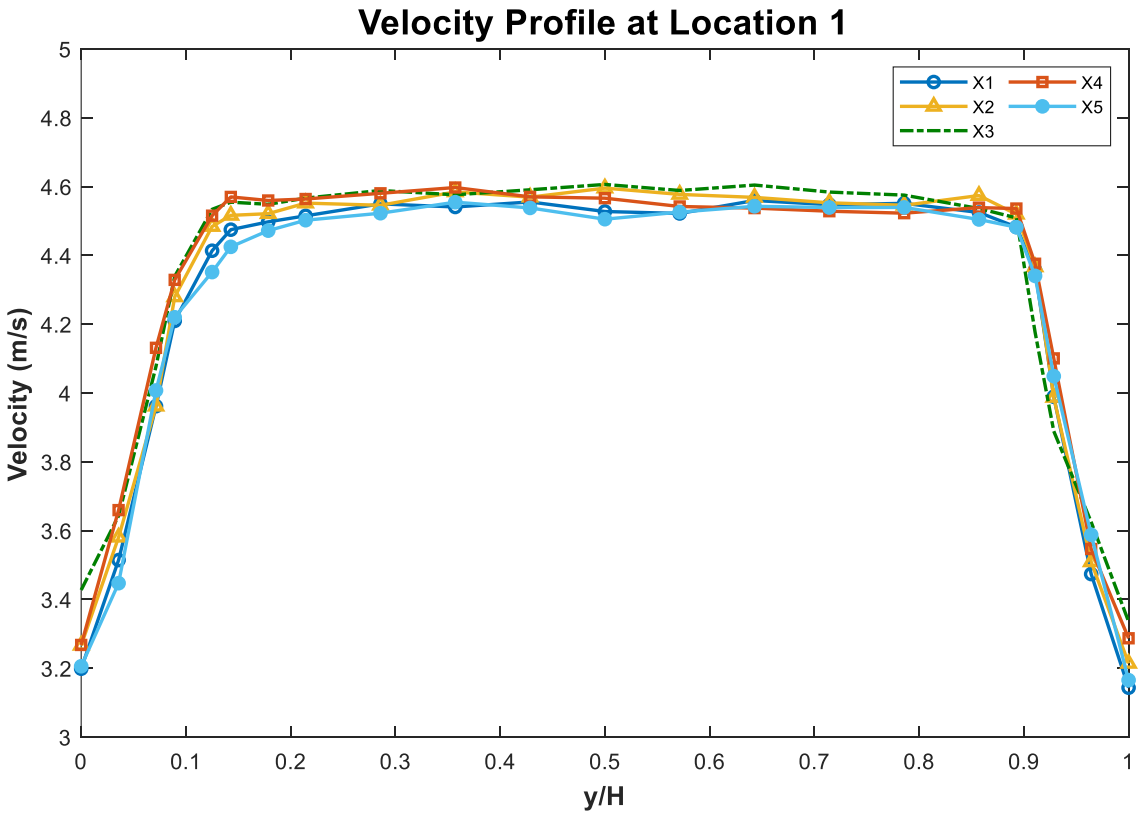

Figure **5-8**: Velocity Profile along y-axis at Location 1.

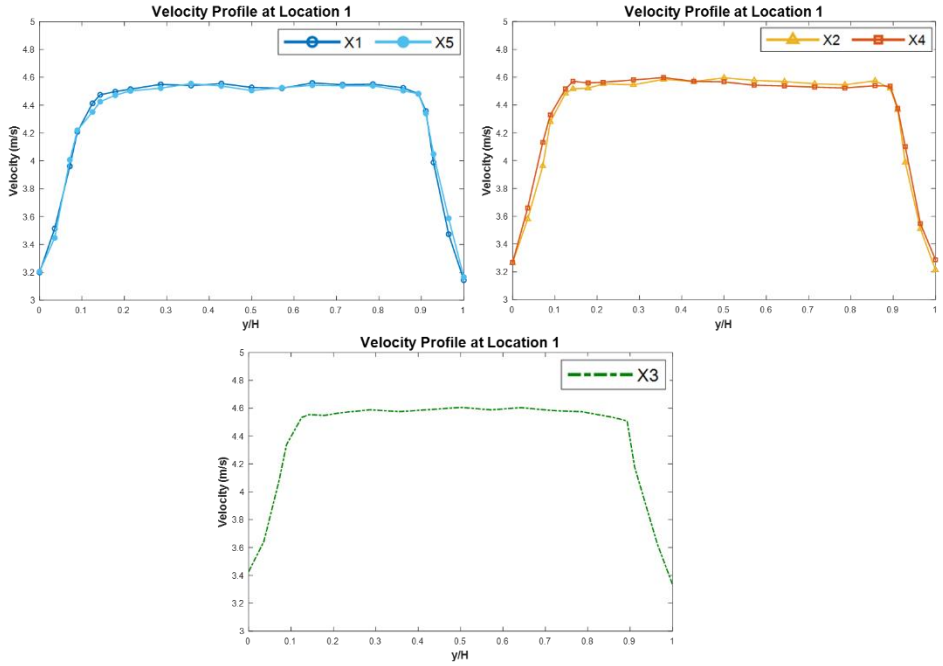

Figure **5-9:** Velocity Profiles at Location 1 along the y-axis showing x1-x5 (top left), x2-x4 (top right), and x3 (bottom) plotted for comparison.

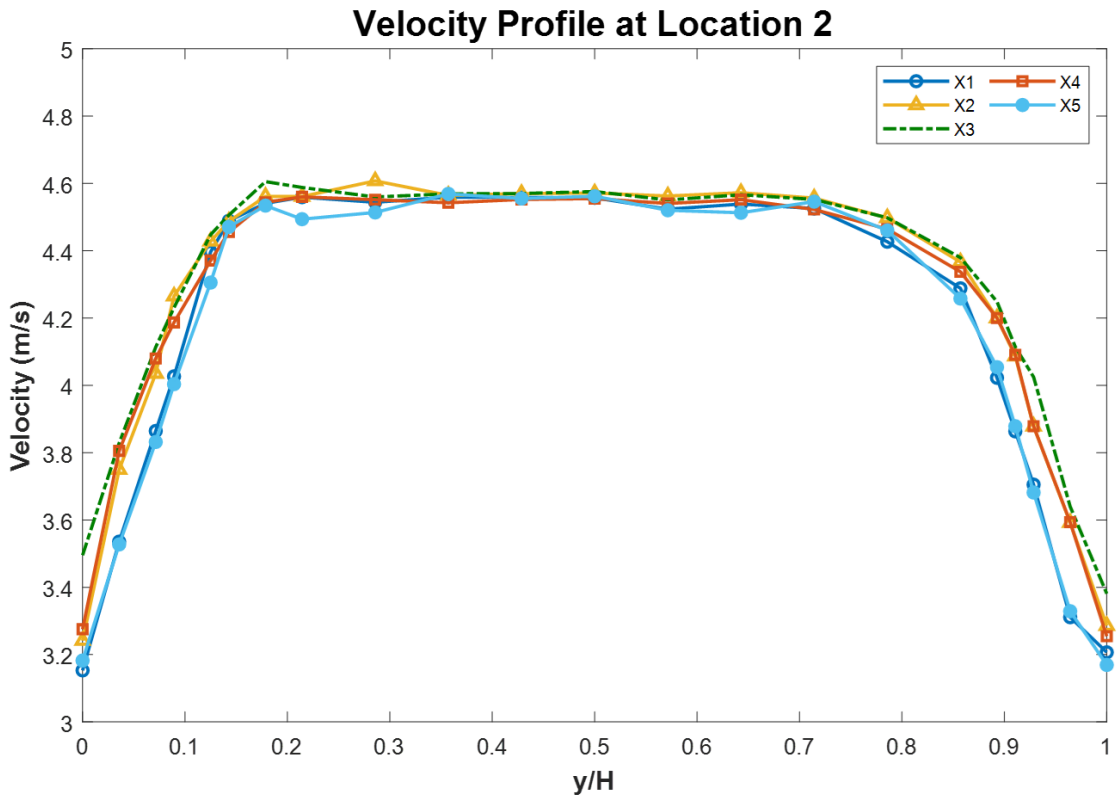

Figure **5-10**: Velocity Profile along y-axis at Location 2.

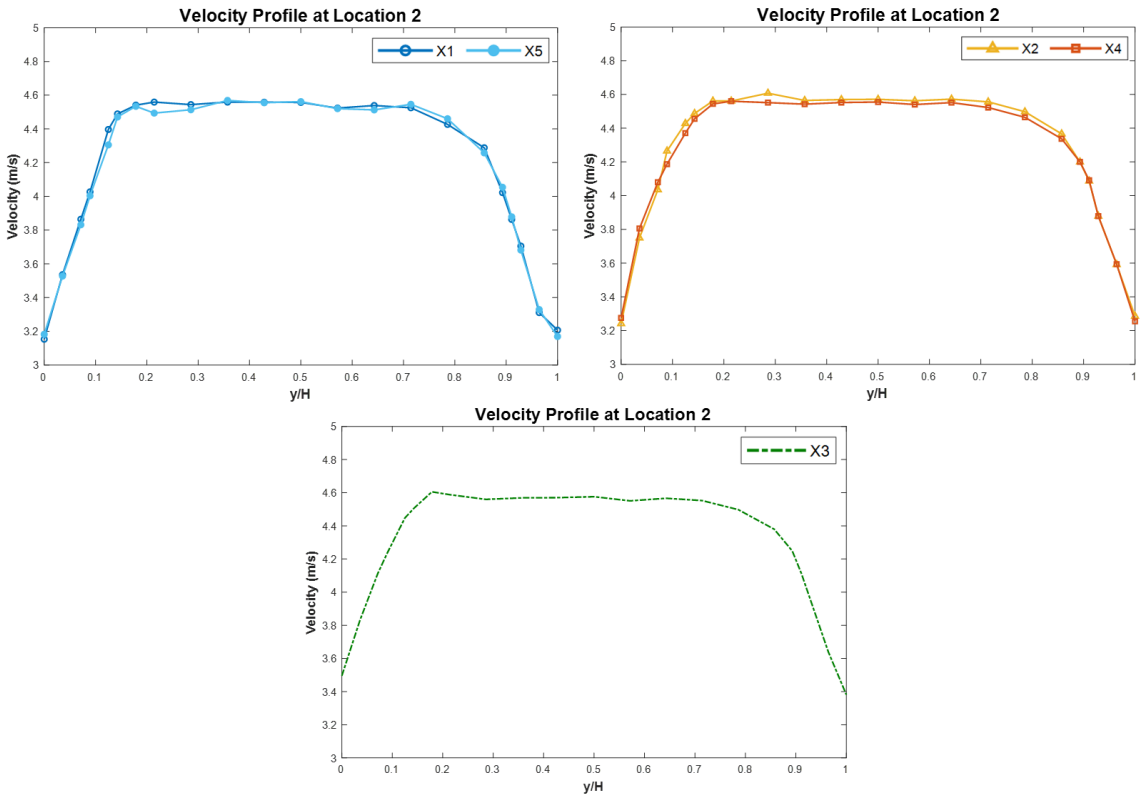

Figure **5-11**: Velocity Profiles at Location 2 along the y-axis showing x1-x5 (top left), x2-x4 (top right), and x3 (bottom) plotted for comparison.

Velocity Profile at Location 2 along different y-points

Velocity Profile at Location 2 at y = 7th and 11th point is presented in Figure 5-13. To obtain a better resolution, pressure measurements for 30 points, equally spaced at 0.35 inches, along the x-direction were collected, as shown in Figure 5-12. It is evident from the graphs that at y = 7th point has a higher velocity than the 11th point. On comparison, from figure 5-13, there is a significant increase in the mean velocity values at both y-locations. The results also show a reduced boundary layer under x/L < 0.1 and 0.15 for 7th and 11th points near the side walls respectively.

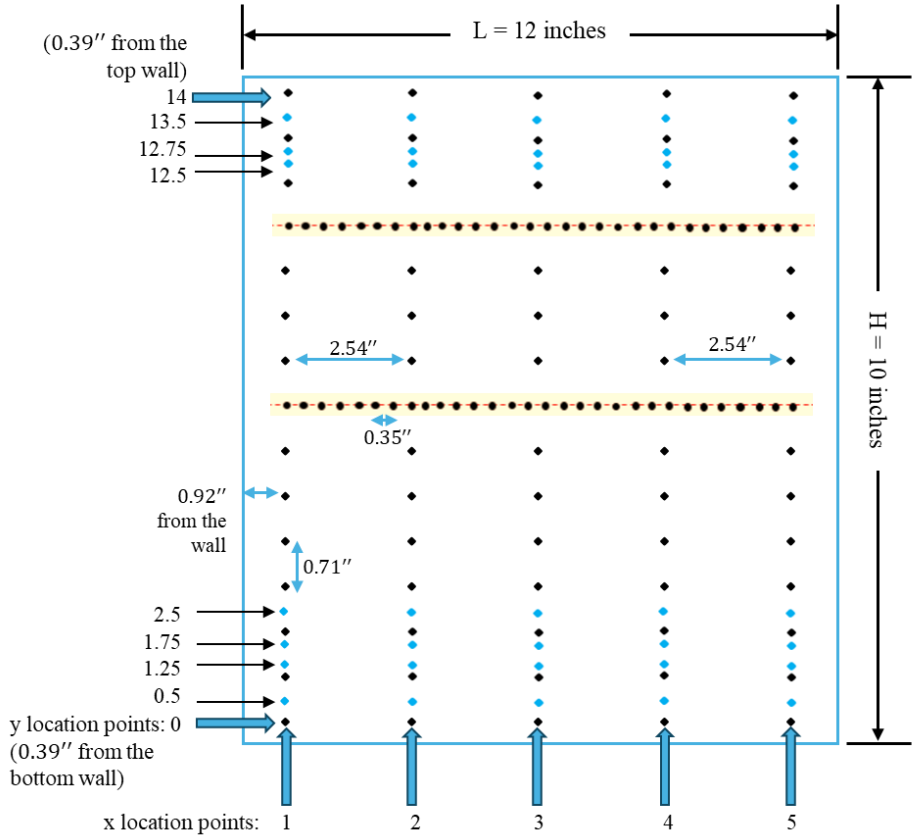

Figure **5-12**: Measurement points at location 2 along different y points, highlighted in yellow.

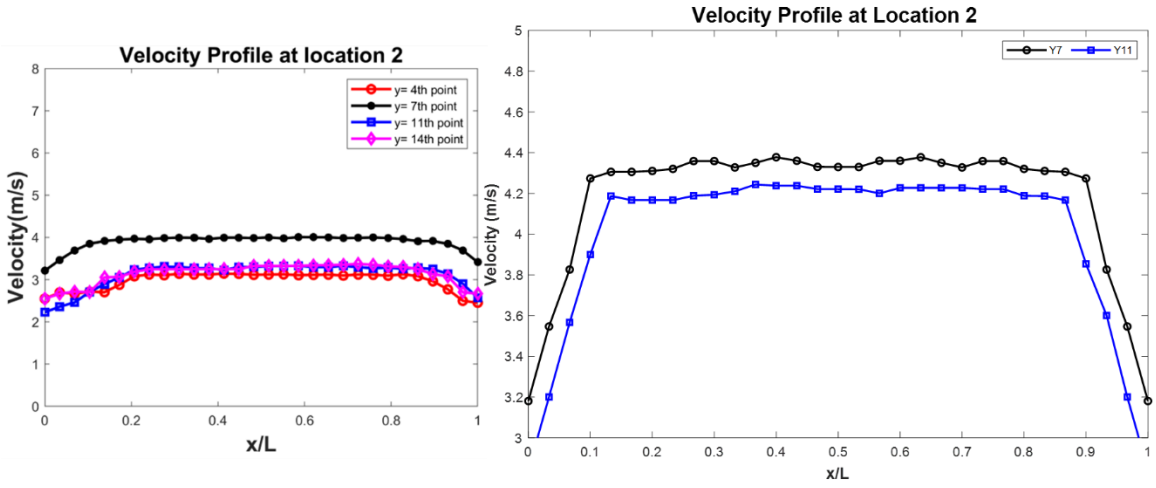

Figure **5-13**: Velocity Profile along x-axis at Location 2 without flanges (left) [9] and with flanges (right).

Turbulence Intensity

The turbulence levels in a wind tunnel are expressed in a percentage scale. Ideally, a 0% turbulence intensity means there are no fluctuations in the flow speed and direction, which is not practically achievable. Usually, the turbulence intensity was calculated as the ratio of the standard deviation of turbulent velocity fluctuations to the average of the velocity over the same period of time [36]. Figure 5-14 displays turbulence intensity profiles at Location 1 and 2 along the y-direction, showing a higher range of turbulence intensity at Location 1 than at Location 2. As expected, the turbulence intensity was higher within the boundary layers, with greater turbulence observed at the lower boundary layer, subsequently a stable region followed, finally before increasing at the top due to the boundary layer effect. At Location 1, the highest turbulence intensity is around 2.9% at the bottom of the test section, while Location 2 records a value of around 4.5% at the top of the test section. On average, the values away from the boundary layer are less than 1% at both locations, which aligns with the ideal achievable value of 2% as suggested [9].

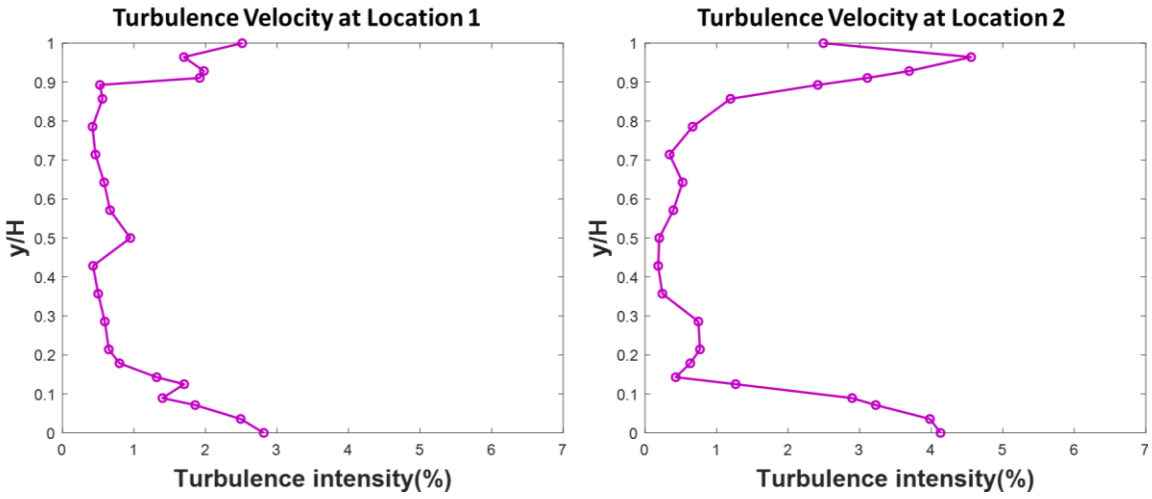

Figure **5-14**: Turbulence Intensity along the y-axis at Location 1 and 2 respectively from left to right.

Impact of the Results

Observations from the results after the addition of the flanges showed improved velocity profiles and decreased turbulence intensity, as expected from a well-functioning wind tunnel [29]. By performing repeatability tests, it was ensured that the wind tunnel yielded consistent accurate results which were reverified by an anemometer. Initially, pressure measurements were recorded for every 1000 frames which is about 322 seconds. The statistical analysis shows that 250 frames (80 seconds) of data is enough to produce the same accurate results as 1000 frame data, as observed from Table 5-2 and Figure 5-4.

Comparing to Wang et al. [9], the velocity profile plots of the y-axis were changed from 0-8 m/s to 3-5 m/s, to closely observe the velocity fluctuations and changes. This enabled a better analysis of the velocity profiles and boundary layer effects at the walls. Specifically, the start of the boundary layer can be visualized better with a close-up view of the graph as shown in Figures 5-15 and 5-16.

At Location 1, the flow does not display characteristics of a fully developed turbulent boundary layer, mainly because of the gap at the entrance of the test section. This gap disrupts the flow, preventing the boundary layer from developing properly at the start. As we move downstream to Location 2, the flow has more distance to evolve and stabilize. By this point, the disturbances introduced by the gap have diminished, allowing the boundary layer to develop more fully. At Location 2, the flow characteristics now resemble those of a fully developed turbulent boundary layer as desired.

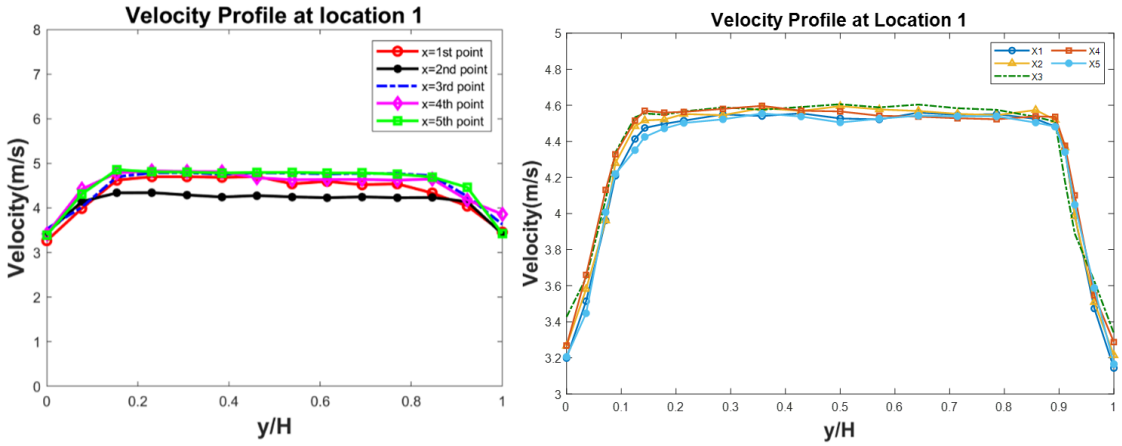

Figure **5-15**: Velocity Profile along y-axis at Location 1 without flanges (left) [9] and with flanges (right).

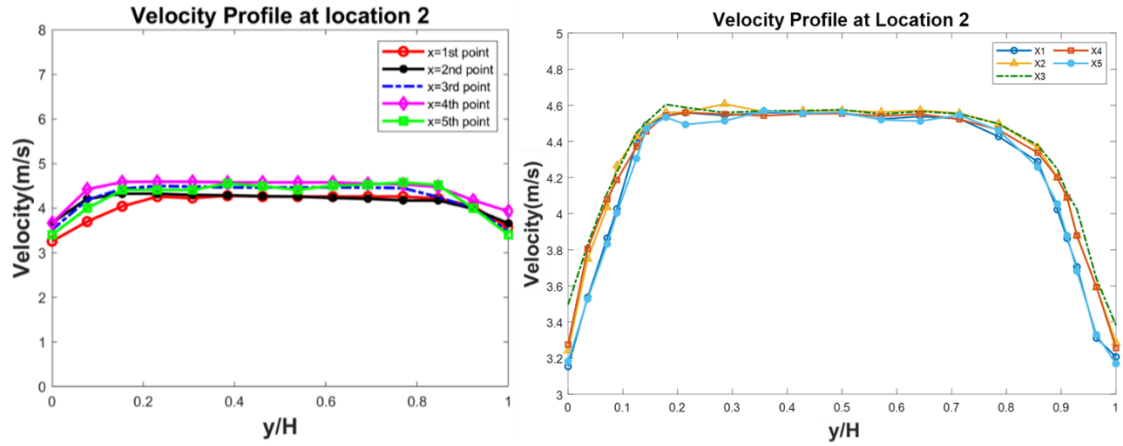

Figure **5-16**: Velocity Profile along y-axis at Location 2 without flanges (left) [9] and with flanges (right).

The turbulence intensity plots indicate significant improvement in the turbulence intensities, even though the turbulence levels at the walls of the test section are higher than average which could be a result of multiple factors that could include design changes, boundary layer management, flow conditioning, and optimizing test conditions, as observed in Figure 5-17. This improvement is likely due to the stable measurements obtained from 250 frames of data after flange addition and better flow properties. These modifications suggest a more uniform and stable flow environment, which is desirable for other research applications.

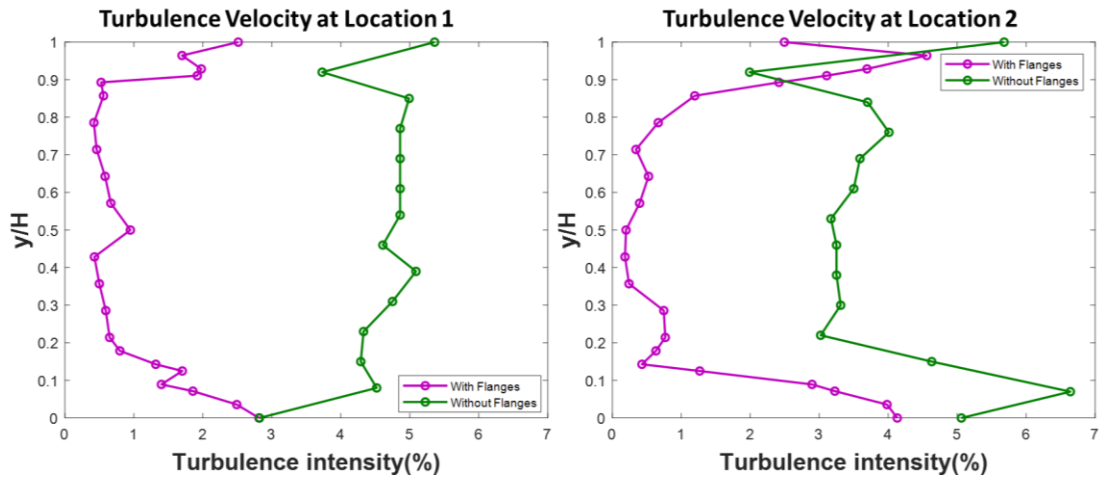

Figure **5-17**: Comparison plots of Turbulence Intensity at Location 1 and 2, with and without flanges [9].

Future Scope and Development

A fully operational, additively manufactured, low speed-wind tunnel was achieved by incorporating flanges at identified locations on the wind tunnel to combat asymmetry and gaps. The final step of permanently sealing the flanges to their respective wind tunnel parts and fastening the flanges with bolts to make sure no gaps exist between the parts is to be done.

Though the wind tunnel yielded accurate results when operating at around 5 m/s, a few design changes could be incorporated in the future. Rather than having the flanges designed as extra components, incorporating them into the part of the wind tunnels wherever needed would prove to be efficient and timesaving while manufacturing. Specifically speaking, the additively manufactured parts could be designed with attached flanges, making it one single part rather than the part itself plus the flange. This would ensure easier part handling and eliminate gaps between the part and the flange.

Since the wind tunnel was designed to be robust and reconfigurable, different co-flow methods can be used to manipulate or control the flow characteristics in the wind tunnel. Though the experiments in this thesis were conducted without a louvre, to enable better flow conditioning in the wind tunnel a new 3D-printed Louvre needs to be incorporated. A louvre with an adjustable guide plate, changing the angles of the plate to guide the airflow and generate diverse velocity profiles in the test section. Additionally, co-flow jets can be introduced as a secondary stream of air parallel to the main flow that can be used for boundary layer control and delayed flow separation. This makes the wind tunnel a flexible and robust tool for conducting research for various applications.

Lastly, Particle Image Velocimetry (PIV) is to be conducted to measure flow fields and provide precise velocity measurements in the test section. A suitable set-up to place the laser to capture the seeded flow particles is necessary to analyze the flow. In this case, a few aligned mirrors should be set up to reflect the laser light onto the test section, rather than installing the laser head on top of the test section, creating a robust and safe system. PIV offers better insights into turbulence, boundary layers, and checks the concordance with the velocity measurements obtained from the pressure measurements.

Appendix A

Lift and Drag Calculation

Consider a free stream velocity (V_∞) approaching the object as shown in Figure A. The resultant force (R), by definition, is the combination of Lift (L), a component of R perpendicular to V_∞ and Drag (D), a component of R parallel to V_∞.

The linear length from the leading to the trailing edge is called the chord (c). Sometimes, when R splits into two: the component of R perpendicular to the chord, is called normal force (N), and a component of R parallel to the chord, called axial force (A).

The angle of attack α is the angle between the chord and V_∞. Drawing geometric relations, to get: $L = N\,cos\,\alpha - A\,sin\,\alpha$ and $D = N\,sin\,\alpha + A\,cos\,\alpha$ [17].

Often, Lift and Drag are expressed as the product of non-dimensionless numbers and other factors that influence the situation for easier calculations. Hence, D = ½ ρv^2. C_D. S and L = ½ ρv^2. C_L. S, where ρ = density, v = velocity, S = reference area, C_D = co-efficient of Drag, and C_L= co-efficient of Lift.

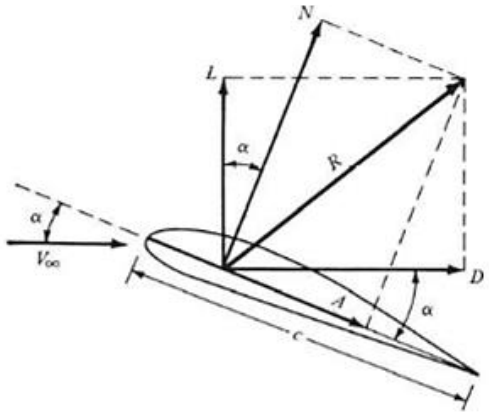

Figure **A**: Resultant aerodynamic forces and its split components on an airfoil structure [17].

Appendix B

Velocity Measurements at Locations 1 & 2

Tables B-1 and B-2 show the measured velocity readings at Locations 1 and 2 derived from the pressure readings from the Scanivalve pressure scanner for different heights along the y-axis at five x-locations.

Table **B-1:** Velocity measurements at Location 1.

Location 1						
Y	Y/H_Total	X1	X2	X3	X4	X5
0.000	0.000	3.199	3.267	3.427	3.268	3.206
0.500	0.036	3.514	3.581	3.643	3.660	3.447
1.000	0.071	3.962	3.962	4.077	4.131	4.007
1.250	0.089	4.209	4.279	4.339	4.329	4.220
1.750	0.125	4.413	4.484	4.534	4.515	4.351
2.000	0.143	4.475	4.516	4.555	4.570	4.425
2.500	0.179	4.497	4.521	4.548	4.559	4.472
3.000	0.214	4.515	4.552	4.566	4.564	4.502
4.000	0.286	4.550	4.546	4.589	4.580	4.522
5.000	0.357	4.541	4.584	4.576	4.597	4.555
6.000	0.429	4.555	4.569	4.591	4.570	4.538
7.000	0.500	4.527	4.595	4.606	4.566	4.505
8.000	0.571	4.522	4.577	4.589	4.542	4.526
9.000	0.643	4.559	4.568	4.604	4.537	4.543
10.000	0.714	4.547	4.553	4.584	4.528	4.539
11.000	0.786	4.551	4.546	4.575	4.523	4.539
12.000	0.857	4.525	4.574	4.536	4.539	4.504
12.500	0.893	4.482	4.519	4.509	4.536	4.482
12.750	0.911	4.358	4.366	4.177	4.376	4.340
13.000	0.929	3.989	3.987	3.889	4.101	4.049
13.500	0.964	3.474	3.509	3.625	3.547	3.588
14.000	1.000	3.144	3.214	3.336	3.287	3.165

Table **B-2:** Velocity measurements at Location 2.

Location 2						
Y	Y/H_Total	X1	X2	X3	X4	X5
0.000	0.000	3.153	3.241	3.495	3.275	3.182
0.500	0.036	3.536	3.750	3.829	3.805	3.527
1.000	0.071	3.865	4.035	4.114	4.080	3.832
1.250	0.089	4.027	4.265	4.231	4.187	4.004
1.750	0.125	4.397	4.428	4.448	4.371	4.305
2.000	0.143	4.489	4.487	4.506	4.456	4.471
2.500	0.179	4.541	4.561	4.605	4.544	4.534
3.000	0.214	4.559	4.561	4.588	4.560	4.494
4.000	0.286	4.544	4.608	4.560	4.552	4.514
5.000	0.357	4.559	4.565	4.569	4.543	4.569
6.000	0.429	4.558	4.570	4.570	4.552	4.555
7.000	0.500	4.557	4.571	4.576	4.555	4.562
8.000	0.571	4.524	4.563	4.551	4.540	4.520
9.000	0.643	4.539	4.572	4.566	4.552	4.513
10.000	0.714	4.526	4.556	4.552	4.523	4.546
11.000	0.786	4.427	4.498	4.498	4.465	4.460
12.000	0.857	4.288	4.366	4.380	4.337	4.258
12.500	0.893	4.022	4.200	4.248	4.200	4.054
12.750	0.911	3.863	4.087	4.114	4.091	3.879
13.000	0.929	3.705	3.879	4.025	3.879	3.682
13.500	0.964	3.311	3.592	3.640	3.593	3.329
14.000	1.000	3.207	3.286	3.381	3.255	3.169

Bibliography

[1] Y. Nagai, A. Okada, N. Miyasato, M. Saitoh, and R. Matsumoto, “Wind Tunnel Tests on Horn-Shaped Membrane Roof Under the Turbulent Boundary Layer,” in *Wind Tunnel Designs and Their Diverse Engineering Applications*, InTech, 2013. doi: 10.5772/54180.

[2] R. S. Van Pelt and T. M., “Portable Wind Tunnels for Field Testing of Soils and Natural Surfaces,” in *Wind Tunnel Designs and Their Diverse Engineering Applications*, InTech, 2013. doi: 10.5772/54141.

[3] A. Almubarak, “Investigation of Drying Mechanism of Solids Using Wind Tunnel,” in *Wind Tunnel Designs and Their Diverse Engineering Applications*, InTech, 2013. doi: 10.5772/54322.

[4] Z. Mo and C.-H. Liu, “Wind tunnel measurements of pollutant plume dispersion over hypothetical urban areas,” *Build Environ*, vol. 132, pp. 357–366, Mar. 2018, doi: 10.1016/j.buildenv.2018.01.046.

[5] M. Marro, J. Leckert, E. Rollier, P. Salizzoni, and C. Bailly, “Wind tunnel evaluation of novel drafting formations for an elite marathon runner,” *Proceedings of the Royal Society A: Mathematical, Physical and Engineering Sciences*, vol. 479, no. 2276, Aug. 2023, doi: 10.1098/rspa.2022.0836.

[6] J. B. Barlow, W. H. Rae, A. Pope, and A. Pope, *Low-speed wind tunnel testing*. Wiley, 1999.

[7] B. Lindgren and A. V Johansson, “Design and Evaluation of a Low-Speed Wind-Tunnel with Expanding Corners,” [Online]. Available: https://api.semanticscholar.org/CorpusID:15356003

[8] L. Cattafesta, C. Bahr, and J. Mathew, “Fundamentals of Wind-Tunnel Design,” in *Encyclopedia of Aerospace Engineering*, Wiley, 2010. doi: 10.1002/9780470686652.eae532.

[9] J. Wang, A. Ul Karim, T. Guimarães, and R. Kunz, “An Additively Manufactured Small Footprint Wind Tunnel for Wall Jet and Particle Scavenging Studies,” in *Volume 9: Fluids Engineering*, American Society of Mechanical Engineers, Oct. 2023. doi: 10.1115/IMECE2023-116730.

[10] J. P. Slotnick *et al.*, “CFD vision 2030 study: a path to revolutionary computational aerosciences,” 2014.

[11] F. D. Witherden and A. Jameson, “Future Directions in Computational Fluid Dynamics,” in *23rd AIAA Computational Fluid Dynamics Conference*, Reston, Virginia: American Institute of Aeronautics and Astronautics, Jun. 2017. doi: 10.2514/6.2017-3791.

[12] D. Graham, J. Dahlin, J. Page, K. Plotkin, and P. Coen, “Wind tunnel validation of shaped sonic boom demonstration aircraft design,” in *43rd AIAA Aerospace Sciences Meeting and Exhibit*, 2005, p. 7.

[13] K. Fujii, “Progress and future prospects of CFD in aerospace—Wind tunnel and beyond,” *Progress in Aerospace Sciences*, vol. 41, no. 6, pp. 455–470, Aug. 2005, doi: 10.1016/j.paerosci.2005.09.001.

[14] R. Temam, *Navier-Stokes equations: theory and numerical analysis*, vol. 343. American Mathematical Soc., 2001.

[15] T.-P. Tsai, *Lectures on Navier-Stokes equations*, vol. 192. American Mathematical Soc., 2018.

[16] Y. Cengel and J. Cimbala, *Ebook: Fluid mechanics fundamentals and applications (si units)*. McGraw Hill, 2013.

[17] J. Anderson, “Fundamentals of Aerodynamics.”

[18] F. K. Owen and A. K. Owen, “Measurement and assessment of wind tunnel flow quality,” *Progress in Aerospace Sciences*, vol. 44, no. 5, pp. 315–348, Jul. 2008, doi: 10.1016/j.paerosci.2008.04.002.

[19] S. Ristić, J. Isaković, B. Ilić, and G. Ocokoljić, “Review of methods for flow velocity measurement in wind tunnels,” *Scientific Technical Review*, vol. 44, pp. 60–71, 2004.

[20] B. Lindgren and A. V Johansson, “Evaluation of the flow quality in the MTL wind-tunnel,” *Flow Facility Design and Experimental Studies of Wall-Bounded Turbulent Shear-Flows*, p. 109, 2002.

[21] P. Moonen, B. Blocken, and J. Carmeliet, “Indicators for the evaluation of wind tunnel test section flow quality and application to a numerical closed-circuit wind tunnel,” *Journal of Wind Engineering and Industrial Aerodynamics*, vol. 95, no. 9–11, pp. 1289–1314, Oct. 2007, doi: 10.1016/j.jweia.2007.02.027.

[22] P. Bradshaw and R. C. Pankhurst, “The design of low-speed wind tunnels,” *Progress in Aerospace Sciences*, vol. 5, pp. 1–69, 1964, doi: https://doi.org/10.1016/0376-0421(64)90003-X.

[23] M. Stewart and K. Arnold, *Surface Production Operations*. Elsevier, 2008. doi: 10.1016/B978-0-7506-7853-7.X5001-7.

[24] M. D. Manshadi, “The importance of turbulence in assessment of wind tunnel flow quality,” *Wind tunnels and experimental fluid dynamics research*, pp. 261–278, 2011.

[25] G. Nader, C. dos Santos, P. J. S. Jabardo, M. Cardoso, N. M. Taira, and M. T. Pereira, “Characterization of low turbulence wind tunnel,” in *XVIII IMEKO World Congress-Metrology for a sustainable development*, 2006.

[26] R. C. Baker, *Flow measurement handbook: industrial designs, operating principles, performance, and applications*. Cambridge University Press, 2016.

[27] J. E. Hardy, J. O. Hylton, T. E. McKnight, C. J. Remenyik, and F. R. Ruppel, *Flow measurement methods and applications*. John Wiley & Sons, 1999.

[28] T. Salzbrunn, H. Leitte, T. Wischgoll, and G. Scheuermann, *The State of the Art in Flow Visualization: Partition-Based Techniques.*, vol. 2008. 2008.

[29] A. Singh and M. Gollner, *Local Burning Rates and Heat Flux for Boundary Layer Diffusion Flames Under Forced Flow*. 2015. doi: 10.13140/2.1.1490.4649.

[30] J. P. Merrison *et al.*, "An environmental simulation wind tunnel for studying Aeolian transport on mars," *Planet Space Sci*, vol. 56, no. 3–4, pp. 426–437, Mar. 2008, doi: 10.1016/j.pss.2007.11.007.

[31] Y. Ohya, T. Karasudani, A. Sakurai, K. Abe, and M. Inoue, "Development of a shrouded wind turbine with a flanged diffuser," *Journal of Wind Engineering and Industrial Aerodynamics*, vol. 96, no. 5, pp. 524–539, May 2008, doi: 10.1016/j.jweia.2008.01.006.

[32] R. F. Huang, G. S. Liu, Y.-K. Chen, W.-Y. Yeh, C.-W. Chen, and C.-C. Chen, "Effects of Flange Size on Dividing Streamlines of Exterior Hoods in Cross Drafts," *J Occup Environ Hyg*, vol. 1, no. 5, pp. 283–288, May 2004, doi: 10.1080/15459620490439045.

[33] J. W. Booth, J. Alperovich, P. Chawla, J. Ma, T. N. Reid, and K. Ramani, "The Design for Additive Manufacturing Worksheet," *Journal of Mechanical Design*, vol. 139, no. 10, Oct. 2017, doi: 10.1115/1.4037251.

[34] S. A. Raj, E. Muthukumaran, and K. Jayakrishna, "A Case Study of 3D Printed PLA and Its Mechanical Properties," *Mater Today Proc*, vol. 5, no. 5, pp. 11219–11226, 2018, doi: 10.1016/j.matpr.2018.01.146.

[35] P. Murdy, J. Dolson, D. Miller, S. Hughes, and R. Beach, “Leveraging the Advantages of Additive Manufacturing to Produce Advanced Hybrid Composite Structures for Marine Energy Systems,” *Applied Sciences*, vol. 11, no. 3, p. 1336, Feb. 2021, doi: 10.3390/app11031336.

[36] A. Pipinato, *Innovative bridge design handbook: Construction, rehabilitation and maintenance*. Elsevier, 2021.